

2

AD-A273 712



FINAL REPORT

OPTICAL INTERFEROMETERS FOR SENSING ELECTROMAGNETIC FIELDS

TO

DEPARTMENT OF THE ARMY
HARRY DIAMOND LABORATORIES
ATTN: JOHN LATESS/SLCHD-NW-ES
WOODBIDGE RESEARCH FACILITY
WOODBIDGE, VA 22191

CONTRACT NO. DAAL02-90-C-0078

FROM

SRICO
664 PETWORTH COURT
POWELL, OH 43065-9398

DTIC
ELECTE
DEC 14 1993
S E D

March 29, 1991

Approved for public release
Distribution unlimited

VIEWS, OPINIONS, AND/OR FINDINGS CONTAINED IN THIS REPORT ARE THOSE OF THE AUTHOR(S) AND SHOULD NOT BE CONSTRUED AS AN OFFICIAL DEPARTMENT OF THE ARMY POSITION, POLICY, OR DECISION UNLESS SO DESIGNATED BY OTHER OFFICIAL DOCUMENTATION.

93 12 13 029

93-30181

**Best
Available
Copy**

Table of Contents

EXECUTIVE SUMMARY	6
INTRODUCTION	7
SUBSTRATE PROPERTIES	12
REFRACTIVE INDEX	13
THEORY OF INTEGRATED OPTIC COMPONENTS	14
OPTICAL WAVEGUIDES	14
Y-BRANCH POWER SPLITTER AND COMBINER	16
DIRECTIONAL COUPLER	16
LINEAR ELECTRO-OPTIC EFFECT	19
MACH-ZEHNDER INTERFEROMETER WITH ELECTRODES	20
DOMAIN INVERSION	24
ELECTRIC FIELD EFFECTS	24
TEMPERATURE GRADIENT EFFECT	24
DOMAIN REVERSAL USING ELECTRON BEAM	25
CONCENTRATION GRADIENT EFFECT	25
PROCESS SEQUENCE FOR CREATING DOMAIN INVERTED REGIONS	27
DOMAIN INVERSION EXPERIMENTS	29
PROTON-EXCHANGE WAVEGUIDE PROCESS	33
PROCESS SEQUENCE	35
ELECTRODE-LESS MACH-ZEHNDER INTERFEROMETER	40
QUADRATURE PHASE BIAS	40
LASER WAVELENGTH	54
DEVICE SENSITIVITY	54
OPTICAL POWER DAMAGE THRESHOLD	55
DEVICE FABRICATION AND PACKAGING	56
SYSTEM ANALYSIS	57
CNR ANALYSIS	57
LINEARITY ANALYSIS	65
SNR ANALYSIS	70
DYNAMIC RANGE ANALYSIS	70
SENSITIVITY ANALYSIS	72
FREQUENCY RESPONSE	75
ELECTRIC FIELD SENSOR CALIBRATION	79
TEM CELL PERFORMANCE	81
DYNAMIC RANGE TESTS	82
APPLICATIONS	85
CONCLUSIONS AND RECOMMENDATIONS	88

Accession For	
NTIS - CRA&I	<input checked="" type="checkbox"/>
DTIC TAB	<input type="checkbox"/>
Unannounced	<input type="checkbox"/>
Justification <i>ll</i>	
By _____	
Distribution / _____	
• • Availability Codes • •	
Dist	Avail and/or Special
<i>A1</i>	

DTIC QUALITY INSPECTED 3

List of Figures

		Page
Figure 1.	Mach-Zehnder interferometer with electrodes	8
Figure 2a.	Photomicrograph of a +Y end-face of a Ti diffused +Z lithium niobate after etching in HF:HNO ₃ ,	10
Figure 2b.	Photomicrograph of a -Y end-face of a Ti diffused +Z lithium niobate after etching in HF:HNO ₃ ,	10
Figure 3.	Schematic of a Y-branch power splitter/combiner	17
Figure 4.	Schematic of a directional coupler power splitter/combiner	18
Figure 5.	Output signal of a symmetric Mach-Zehnder interferometer	23
Figure 6.	Process sequence for creating domain inversion in a +Z oriented lithium niobate crystal	28
Figure 7.	-Z oriented LiNbO ₃ , diffused with 1000Å of Ti at 1025 C for 8 hours. The crystal surface is subsequently etched in HF:HNO ₃ , at 80 to 90 C for 3 minutes	29
Figure 8.	+Z oriented LiNbO ₃ , crystal diffused with 1000Å of Ti at 1025 C for 8 hours and subsequently etched in HF:HNO ₃ , at 80 to 90 C for 3 minutes	30
Figure 9.	+Z oriented LiNbO ₃ , diffused with 500Å of Ti at 1025 C for 8 hours and subsequently etched in HF:HNO ₃ , at 80 to 90 C for 3 minutes	30
Figure 10.	+Z oriented LiNbO ₃ , diffused with 1000Å Ti at 1050 C for 8 hours and subsequently etched in HF:HNO ₃ , at 80 to 90 C for 3 minutes	31
Figure 11.	+Z oriented LiNbO ₃ , showing a 9 micron channel diffused with 1000Å titanium at 1025 C for 8 hours and subsequently etched in HF:HNO ₃ ,	32
Figure 12.	Process sequence for creating proton-exchange waveguide in lithium niobate	36

Figure 13.	Schematic of an electrode-less Mach-Zehnder interferometer	37
Figure 14.	Schematic of a tapered Ti region to overcome the effects of abrupt steps in the lower leg of the Mach-Zehnder interferometer	39
Figure 15.	Cross section of the proton-exchange waveguide in the upper leg of the interferometer	43
Figure 16.	Three layer model of the PE waveguide in the upper leg of the interferometer	43
Figure 17.	Cross section of the proton-exchange waveguide in the Ti diffused domain inverted region in the lower leg of the interferometer	44
Figure 18.	Three layer model of the PE/Ti waveguide region in the lower leg of the interferometer	44
Figure 19.	Four layer model of the PE/Ti diffused waveguide region	44
Figure 20.	Plot of the effective index as a function of δ , relative to the value for $\delta = 0$	49
Figure 21.	Plot of the change in effective index between the two arms of the interferometer and the interferometer phase change as function of wavelength over a limited range	52
Figure 22.	CNR for single-ended detection	62
Figure 23.	Mach-Zehnder interferometer with dual-balanced detector at the output	63
Figure 24.	CNR for dual-balanced detection	64
Figure 25.	Modulation ratio as a function of phase bias Peak phase deviation = 0.1 radian	67
Figure 26.	Modulation ratio as a function of phase bias Peak phase deviation = 0.25 radian	68
Figure 27.	Interferometer response at quadrature bias	69
Figure 28.	Relative signal levels for 1mW received power	71
Figure 29.	Relative signal levels for 10mW received power	71

Figure 30.	Periodic phase reversal technique to increase the device operating frequency to 30 GHz	77
Figure 31.	Schematic for calibrating the electric field sensor	80
Figure 32.	Electric field and peak phase modulation depth as a function of TEM cell drive power	83
Figure 33.	Schematic of a configuration for the remote measurement of electric field or voltage	87

List of Tables

		Page
I.	Sensor specifications	11
II.	Properties of lithium niobate	12
III.	3-layer calculation of effective indices	47
IV.	Effective index calculation of channel waveguide effective indices	50
V.	CNR for single-ended detection	59
VI.	CNR for dual-balanced detection	60
VII.	Sensitivity calculations	74

EXECUTIVE SUMMARY

This report summarizes the work performed by SRICO under contract number DAAL02-90-C-0078 sponsored by the U.S. Army Harry Diamond Laboratories. This was a Phase I research program entitled "Optical Interferometers for Sensing Electromagnetic Fields". The overall goal of the program was to determine the feasibility of manufacturing a nonmetallic electromagnetic field sensor to measure wideband transient electromagnetic responses using integrated optical waveguide interferometers. This nonmetallic design minimizes the perturbation on the electric fields and allows the accurate measurement of large fields.

The integrated optic device makes use of a Mach-Zehnder interferometer in a lithium niobate electro-optic crystal material. The electric field sensor uses the electro-optic properties of lithium niobate to modulate the phase of the light propagating in each arm of the Mach-Zehnder interferometer. This phase modulated optical signal is converted to intensity modulation at the output of the interferometer.

Conventional, integrated optic electric field sensors utilize a dipole antenna connected to the metallic electrodes on the waveguide channels to apply voltage of opposite polarities on the two channels. This is an indirect method of measuring the electric field.

The need for metal electrodes could be eliminated if one leg of the interferometer were to be oppositely poled. SRICO successfully demonstrated a selective reverse poling of one leg of the interferometer using high temperature diffusion of titanium into lithium niobate. A series of experiments were performed to determine the optimum diffusion conditions to obtain 100% reverse poling of one waveguide channel without affecting the rest of the crystal substrate. The optical waveguide is then fabricated by a low temperature proton-exchange process.

Analysis of the sensor system indicates that it can detect electromagnetic fields with a dynamic range greater than 40 dB and a signal bandwidth of 3 GHz. The sensor could be designed to operate from DC to 3 GHz or as a passband device operating at a frequency as high as 30 GHz.

The sensor is packaged with optical fibers for input and output. The optical fibers enable remote measurement of the field from a safe distance of 100 meters.

The electric field sensor developed during this Phase I program has been shown to be feasible and a prototype sensor instrument has been proposed for a Phase II SBIR program.

INTRODUCTION

Fiber optic technology has made great strides in the last two decades, especially for applications in telecommunications and sensors. Fiber optics provides the advantages of secure transmission, immunity to EMI/EMP, wide bandwidth, low weight and long link length on the order of several kilometers. Optical fibers can be combined with integrated optical devices to yield miniature, compact and rugged components for sensing applications.

In addition to their compatibility with optical fibers, other advantages of optical waveguide devices include permanent alignment of components, compatibility with existing planar processing technology, diffraction-free beam propagation, low voltage and/or power requirements, high modulation rates and freedom from electromagnetic interference. Optical fibers can be directly attached to optical waveguides without the need for any bulk optic components such as lenses and polarizers. Integrated optical sensors could, therefore, be made compact, rugged and reliable to withstand severe military environments.

One popular integrated optical waveguide device is the Mach-Zehnder interferometer that is capable of modulating the intensity of the optical beam when a voltage or an electric field is applied to an electro-optic crystal. The structure of a Mach-Zehnder interferometer shown in Figure 1, consists of an input Y-branch, an output Y-branch, and two parallel waveguide channels that connect the two Y-branches. By positioning appropriate electrodes on or near the parallel waveguide channels, this device can sense voltage or electric field¹. Typically, in a conventional electromagnetic field sensor, an external field to be measured is picked up by an antenna and converted to a voltage which is then applied to the electrodes on the crystal. The electrodes are connected so that the two parallel channels experience opposite polarities, thereby, leading to a net phase shift of twice the phase shift per channel.

In a variety of applications that require the measurement of electromagnetic fields, the presence of the metal electrode tends to disturb the electric field under measurement. In severe cases, the close proximity of the electrodes could create arcing, thus creating a short circuit. The electrodes also tend to limit the frequency response of the sensor due to the capacitive nature of the electrical circuit. It would, therefore, be ideal to develop an electric field sensor that does not require any metal electrodes. Such a device could be accomplished if one leg of the

¹C.H. Bulmer and W.K. Burns, "Linear interferometric modulators in Ti:Lithium Niobate", Journal of Lightwave Technology 2, pp. 512-521 (1984).

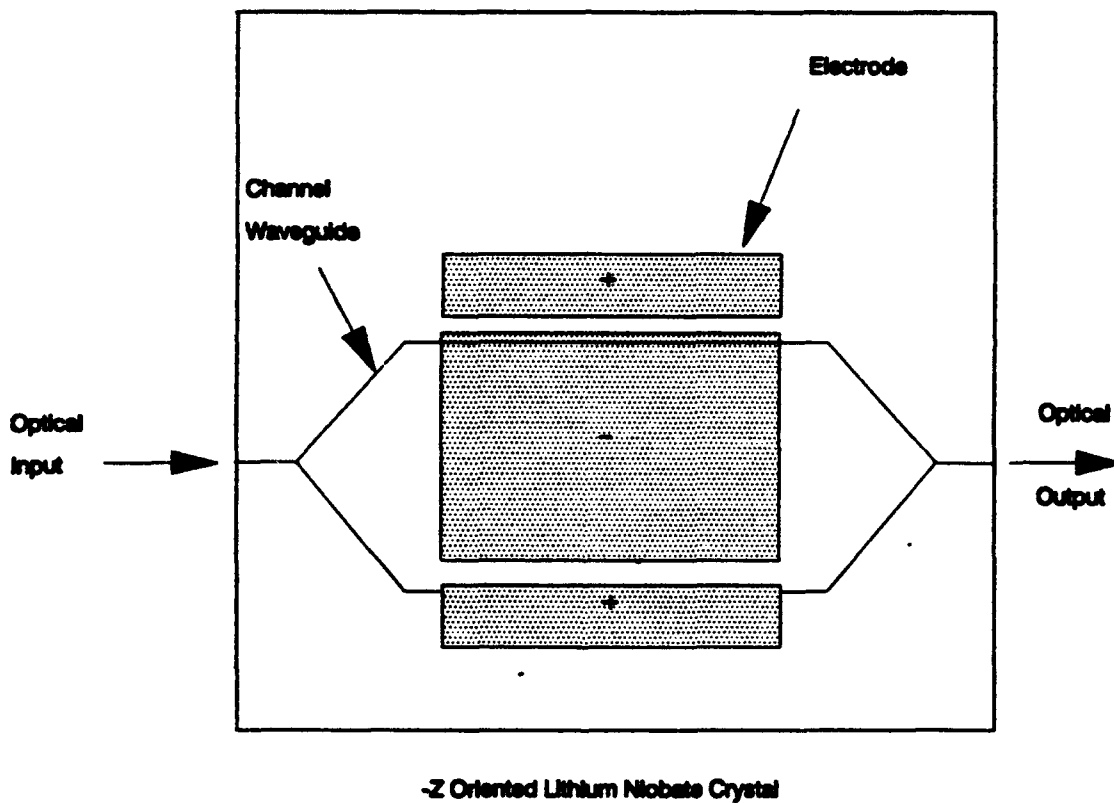


Figure 1. Mach-Zehnder interferometer with electrodes

Mach-Zehnder were to be poled in the opposite direction to that of the rest of the crystal and the waveguide. The device thus created would be more accurate in the measurement of the electromagnetic fields.

We have developed a unique method of creating an electrode-less Mach-Zehnder interferometer in lithium niobate by combining a titanium diffusion step followed by a proton-exchange process. The titanium diffusion in selected sections of the crystal in a +Z oriented substrate is capable of reverse poling that section². Subsequently, the Mach-Zehnder waveguide structure is created at a low temperature by using proton-exchange waveguide techniques³. This technique thus avoids the conventional approach used in poling a crystal which consists of heating the crystal near its Curie temperature, and in some instances beyond its Curie temperature, while applying an electric field^{4,5}. Such an approach would be very cumbersome and expensive.

During the Phase I of this SBIR program, SRICO successfully demonstrated selective domain reversal of a waveguide channel in a +Z oriented LiNbO₃. Figures 2a and 2b show the +Y and -Y end-faces of a 9 μm wide Ti diffused channel in a +Z LiNbO₃ substrate. The end-faces of the substrate were polished and etched in a solution of HF and HNO₃.

The property of this etch solution is such that the +Y face is etched and leaves the -Y face intact. The half-moon shaped region is the Ti diffused region. In Figure 2a, the Ti diffused region remains smooth whereas the background, the +Y face, shows etch pits. This indicates that the end-face associated with the Ti diffused region is converted to -Y orientation, i.e. the Ti diffused channel is domain inverted to -Z in the +Z substrate.

²S. Miyazawa, "Ferroelectric domain inversion in Ti diffused lithium niobate optical waveguide," *Journal of Applied Physics* **50**, pp. 4599-4603 (1979).

³J.L. Jackel et.al., "Proton exchange for high index waveguides in lithium niobate," *Topical Meeting on Integrated and Guided-Wave Optics*, Pacific Grove, CA, 1982.

⁴K. Nassau et.al., "Ferroelectric lithium niobate. 2. Preparation of single domain crystals", *J. Phys. Chem. Solids* **27**, pp. 989-996 (1966).

⁵M. Tasson et.al., "Piezoelectric study of poling in lithium niobate crystals at temperature close to the Curie point", *Ferroelectrics* **13**, pp. 479-481 (1976).



Figure 2a
+Y End-Face

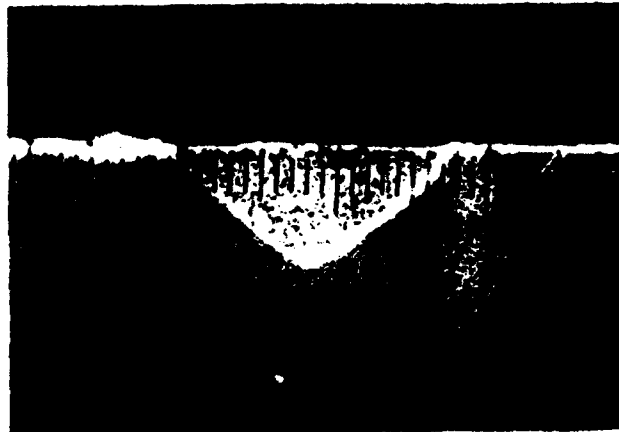


Figure 2b
-Y End-Face

Figures 2 a,b. Photomicrographs of +Y and -Y end-faces of a Ti diffused +Z oriented LiNbO₃, after etching in HF:HNO₃,

The features on the -Y end-face are exactly the opposite as shown in Figure 2b. In Figure 2b, the Ti diffused region exhibits etch pits whereas the background, the -Y face, remains smooth.

This domain inversion selectively occurs only in the Ti diffused regions. We have also demonstrated that 100% domain inversion can be achieved by choosing appropriate diffusion conditions. There is, therefore, no degradation in the electro-optic properties of the crystal. We expect the electrode-less device to have identical performance characteristics as the push-pull electroded Mach-Zehnder interferometer.

The specifications for the electric field sensor provided in the following page are based on our study during the Phase I of the SBIR program. The performance of the sensor for a device operating at 1, 3 and 30 GHz are presented in Table I.

Table I

SENSOR SPECIFICATIONS

Halfwave Voltage, V _π	Volts	40	50	67
Substrate Thickness	mm	.5	.5	.5
Number of Segments	--	1	1	10
Segment Interaction Length	mm	25	20	2.3
Device Bandwidth	GHz	DC to 1	DC to 3	30 ± 1.5
P _π	mW	1	2	4
P _{in}	mW	>2	>4	>8
P _{source}	mW	5	10	10
Wavelength	μm	1.3	1.3	1.3
Signal Bandwidth	GHz	1	1	1
Dynamic Range	dB	48.6	50.83	52.82
E _{min}	V/m	570	490	460
E _{max}	V/m	1.5 x 10 ⁵	1.7 x 10 ⁵	2.0 x 10 ⁵

SUBSTRATE PROPERTIES

The substrate material is LiNbO₃.

The LiNbO₃ crystal has a threefold axis of symmetry which places it in the trigonal (rhombohedral) point group 3m, space group R3c. Some of the physical properties of LiNbO₃ are shown in Table II⁶.

Table II

Properties of Lithium Niobate

Physical Parameter	Value	Units
Density	4.64	g/cm ³
Melting Point	1253	C
Curie Temperature Stoichiometric Congruent	1210 1150	C C
Moh Hardness	5	--
Thermal Conductivity	10 ⁻¹²	cal/cm.S.C
Pyroelectric Coefficient	4 @ 300K	nC/cm ² /C
Resistivity	10 ¹³ @ 24C 5 x 10 ⁸ @ 400C 140 @ 1200C	Ohm-cm
Relative Permittivity	$\epsilon_{11}/\epsilon_0 = 85.2$ $\epsilon_{33}/\epsilon_0 = 28.7$ $\epsilon_{11}/\epsilon_0 = 44.3$ $\epsilon_{33}/\epsilon_0 = 27.9$	Clamped Clamped Unclamped Unclamped

⁶R.S. Weis and T.K. Gaylord, "Lithium niobate: Summary of physical properties and crystal structure", Applied Physics A37, pp. 191-203 (1985).

REFRACTIVE INDEX

The refractive index of the crystal depends on crystal composition. LiNbO_3 , commercially available is congruent melting, having a Li/Nb mole ratio of 0.946 (or 48.6 mol % of LiO_2). Also, being a negative uniaxial crystal, the extraordinary index n_e is less than the ordinary refractive index n_o .

The refractive index values reported at the wavelength of 633 nm and at $T = 24.5 \text{ C}$ are:

n_o , Stoichiometry	2.2005	n_e , Congruent Melting	2.2028
n_o , Stoichiometry	2.291	n_e , Congruent Melting	2.2866

The index of refraction dependence on temperature is given in the paper by Boyd et.al.⁷

Lithium niobate is a very important integrated optic waveguide material. This is a ferroelectric material. It is characterized by high piezoelectric, electro-optic, pyroelectric and photo-elastic coefficients. It has an excellent acousto-optic figure of merit. In this program, we make use of the high transparency of this crystal material in the wavelength of interest (visible to near IR), the ability to create excellent low loss waveguides and a high electro-optic coefficient of the crystal material.

Below its Curie temperature of 1210 C, the crystal is in its ferroelectric phase; and above T_c , it is in its paraelectric phase. Since we will not be operating the crystal during processing or device operation beyond its Curie temperature, we shall limit our discussion to its ferroelectric phase.

In its ferroelectric phase, it consists of planar sheets of oxygen atoms in a distorted hexagonal close-packed configuration. The octahedral interstices formed in this structure are one third filled by lithium atoms, one third filled by niobium atoms, and one-third vacant. In the +C direction, the atoms occur in the interstices in the following order: ____, Nb, vacancy, Li, Nb, vacancy, Li, _____. (See Fig. 1, Weis and Gaylord).

This is a member of the trigonal crystal system as it possesses a threefold rotation symmetry about its C axis. It also exhibits a mirror symmetry about three planes that are 60 degrees apart and intersect forming a threefold rotation axis. (See Fig. 3, Weis and Gaylord).

⁷G.D. Boyd et. al., "Refractive index as a function of temperature in LiNbO_3 ", J. Appl. Phys. 38, pp. 1941-1943 (1967).

THEORY OF INTEGRATED OPTIC COMPONENTS

In this section we provide a brief overview of the physical principles of the integrated optic components that make up the electric field sensor. This includes a discussion about:

- The integrated optical waveguide that will be used to confine the optical beam within the substrate material;
- The integrated optical waveguide Y-branch and directional coupler that will be used in splitting and combining a guided optical wave propagating in the waveguide;
- The electro-optic effect that will be used to change the index of refraction of the substrate material and thereby affect the phase of the optical beam propagating in the optical waveguide;
- The Mach-Zehnder interferometer that will convert the phase shift produced by the electro-optic effect to an intensity variation in the light output, thus enabling the detection of an external electric field.

OPTICAL WAVEGUIDES

Optical waveguides form the basic building block of integrated optical devices. The waveguide is used to confine the light beam in a few micron layers within the substrate. A layer of material can act as an optical waveguide if it satisfies the following requirements:

- The waveguide layer (the core) and the substrate material (the cladding) must be transparent at the wavelength of the optical beam;
- The waveguide layer must have an index of refraction higher than its surrounding materials;
- The waveguide layer must have a minimum thickness to propagate at least one guided mode.

An integrated optical waveguide device incorporates a planar layer or a channel formed in a material adapted to a specific application. The class of materials of interest for optical waveguide devices includes glass, silica, or silicon, polymers, III-V semiconductors, dielectrics, such as potassium titanyl phosphate (KTP) and ferroelectrics, such as lithium niobate and lithium tantalate. Optical waveguide device materials such as KTP,

lithium niobate and lithium tantalate utilize the electro-optic properties of the crystal material for modulation and switching of the guided beam.

Some of the techniques used to fabricate optical waveguides are diffusion, deposition and ion-exchange.

In the diffusion process, a thin layer of material is deposited on top of the substrate material and diffused into the material at elevated temperatures. For example, an optical waveguide is formed in a lithium niobate substrate by diffusing a layer of titanium at about 1025 C.

In the deposition process, a layer of high index material is deposited on top of the substrate material. The deposition processes typically used are sputtering, evaporation and plasma deposition. For example, a layer of silicon nitride when deposited on top of an oxidized silicon substrate could act as an optical waveguide.

Ion-exchange waveguides are formed by immersing a substrate material in suitable solutions such that ions in the solution enter the substrate to increase the refractive index of the ion-exchanged region. For example, by immersing soda lime glass in a silver nitrate solution, a waveguide layer is formed in the glass substrate when the silver ions enter the substrate and replace the sodium ions in the glass.

There are two basic types of optical waveguides. The first type is the planar waveguide which covers the entire top surface of the substrate material. The waveguide is bounded only in one direction by the thickness of the waveguide layer. The optical beam is capable of propagating in any direction in the plane of the waveguide. This planar waveguide geometry is used in acousto-optic devices in which the guided wave is diffracted at many different angles by the acoustic surface waves^{*}.

The second type of optical waveguide is the channel waveguide in which the light beam is confined to propagate in a specific path defined by the channel. The waveguide is bounded in both the thickness and the width, and the light beam propagates along the length of the channel. The light beam is thus well confined within the channel region. The channels are fabricated by confining the deposition or diffusion process to the required width by using the photolithographic process. Channel waveguides are used to direct the optical beam to specific locations by forming the desired

^{*}C.S. Tsai, et. al., "Wide-band guided-wave acousto-optic Bragg diffraction and devices using multiple tilted surface acoustic waves", Proc. IEEE 64, 318 (1976).

optical circuits on the substrate. The electric field sensor under development utilizes channel waveguides in a lithium niobate electro-optic crystal material.

Y-BRANCH POWER SPLITTER AND COMBINER

The Mach-Zehnder interferometer uses a Y-branch at its input and output. At the input, the Y-branch acts as a power divider to excite the two legs of the interferometer. For a perfectly symmetric junction, the power will be divided equally between the two arms as shown in Figure 3a. Any departure from symmetry will result in unequal power splitting.

At the output of the Mach-Zehnder, the Y-branch acts to combine the light propagating in the two legs of the interferometer. For equal inputs into the two arms, the output will vary from zero to the sum of the two input intensities, depending on the relative phase of the two inputs. If the two inputs are equal and in phase, the output of the Y-branch will be equal to the sum of the two input intensities as shown in Figure 3b. But, if the amplitude of the two inputs are equal but opposite in phase, the output of the Y-branch will be zero. The energy that does not reach the output arm is radiated into the substrate as shown in Figure 3c. In principle, the Y-branch is a four port device -- the three arms of the Y-branch account for three ports and the substrate is the fourth port.

DIRECTIONAL COUPLER

Another waveguide component that could be used as a power splitter or a combiner is a directional coupler shown in Figure 4. A directional coupler consists of two parallel channel waveguides fabricated close together such that the two waveguides interact with each other. The evanescent optical fields in the two waveguides overlap such that the energy is transferred between each other. The coupling of light between the two waveguides depend on:

- The separation between the two waveguides;
- The length over which interaction takes place between the two channel waveguides;
- The index of refraction of the waveguide and the surrounding medium.

The directional coupler is a four port device. One major difference between the directional coupler and the Y-branch is that all four ports of the directional coupler are waveguides. Hence, there is no energy wasted in the substrate due to radiation.

Figure 3a. Y-Branch Power Splitter

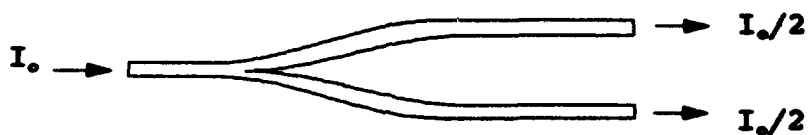


Figure 3b. Y-Branch Power Combiner
The two inputs are equal and in phase

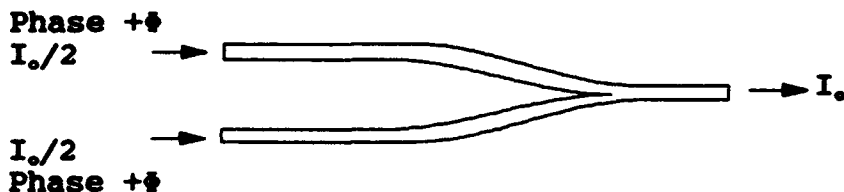


Figure 3c. Y-Branch Power Combiner
The two inputs are equal but out of phase

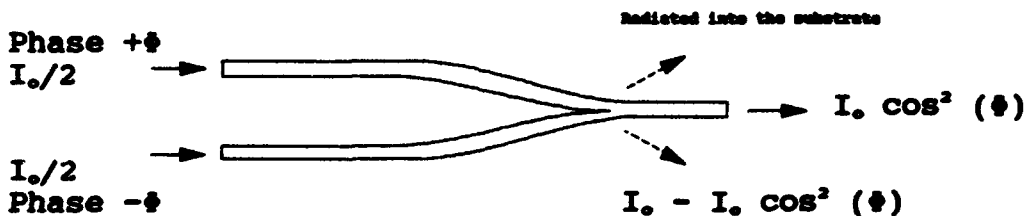


Figure 3. Y-Branch Power Splitter and Combiner

Figure 4a. Directional Coupler - Splitter

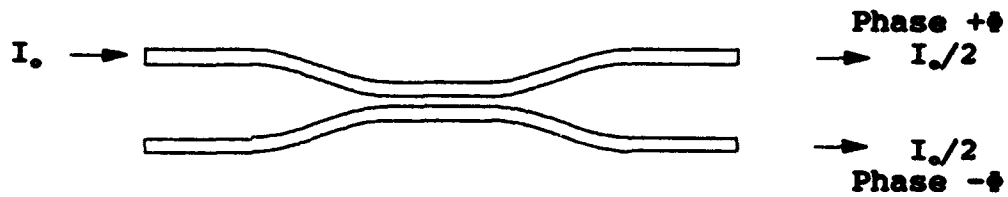


Figure 4b. Directional Coupler - Combiner

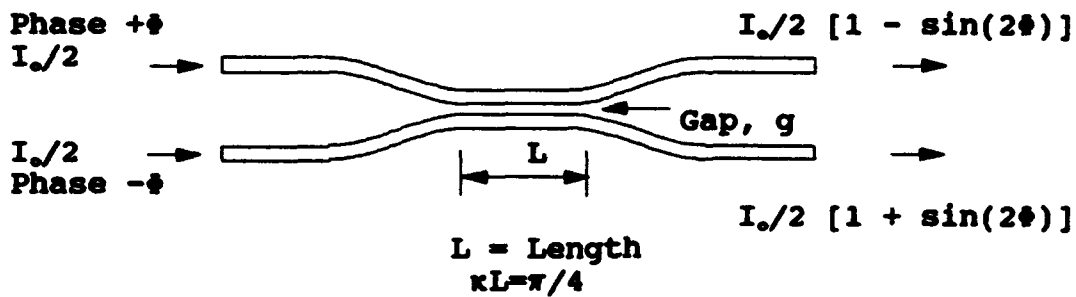


Figure 4. Directional Coupler Power Splitter/Combiner

The directional coupler could therefore be used to replace the output Y-branch to recombine the optical signal without any loss of energy. The directional coupler could be designed and fabricated such that the two output ports have equal intensities. One additional feature of the directional coupler is that the two outputs are always out of phase. We will later make use of this property of the directional coupler to increase the carrier-to-noise ratio of the electric field sensor.

LINEAR ELECTRO-OPTIC EFFECT

The key parameter of interest for this interferometer device is the linear electro-optic effect, also known as the Pockels Effect. The linear electro-optic effect is manifested in a non-centro symmetric crystal when an electric field is present. The relationship between the refractive index change and the electric field is

$$\Delta \left(\frac{1}{n^2} \right)_{ij} = \sum_k r_{ijk} E_k \quad (1)$$

where, $\Delta(1/n^2)_{ij}$ is the second-rank tensor describing the change in relative permittivity, E_k is the k-th component of the electric field vector and r_{ijk} is the third-rank linear electro-optic coefficient tensor. The electro-optic tensor of 27 elements can be reduced to a 6x3 matrix. Lithium niobate has only four independent coefficients (r_{31} , r_{22} , r_{13} and r_{33}). The r_{ijk} tensor in reduced subscript notation is given by:

$$r_{ijk} = \begin{vmatrix} 0 & -r_{22} & r_{13} \\ 0 & r_{22} & r_{13} \\ 0 & 0 & r_{33} \\ 0 & r_{42} & 0 \\ r_{42} & 0 & 0 \\ -r_{22} & 0 & 0 \end{vmatrix}$$

$$\begin{aligned} r_{22} &= 6.8 \times 10^{-12} \text{ m/V}, & r_{13} &= 10 \times 10^{-12} \text{ m/V}, \\ r_{33} &= 30.8 \times 10^{-12} \text{ m/V}, & r_{31} &= 32.6 \times 10^{-12} \text{ m/V}. \end{aligned}$$

These values are at the wavelength of 633 nm.

MACH-ZEHNDER INTERFEROMETER WITH ELECTRODES

A symmetric Mach-Zehnder (MZ) interferometer device is shown in Figure 1. This is an electroded device. This device, when driven by a dipole antenna, would function as an electric field sensor. The dipole antenna converts the electric field to a voltage output. This voltage is applied to the electrodes on the device. The electrode arrangement shown in Figure 1 is for a -Z oriented LiNbO₃ crystal.

The waveguide structure shown consists of an input channel that propagates the light into the input Y-branch. At the Y-branch, the light is equally split between the two channels. The two channels branch out at an angle of one degree to a separation of 50 μm. The two channels are bent so that they are parallel to each other over the length L. The two parallel channels then recombine at the output Y-branch and transmit the recombined light into the output port. In the symmetric device shown, the optical path lengths associated with the light in the upper and lower half of the MZ interferometer are equal. In the absence of an external voltage, the two optical beams experience equal phase shift, leading to a net phase shift of zero.

The electrodes are placed such that the electric field generated in the crystal due to the applied voltage is in the Z direction. The electric field is oppositely directed in the two legs of the interferometer.

The effect of this electric field is to change the refractive index of the material through the linear electro-optic effect. Since the electric field is only in the Z direction, $E_x, E_y = 0$. Only E_z is a non-zero component of the electric field vector. The index change along each direction can be calculated using the electro-optic tensor r_{ijk} . If we let 1,2,3 correspond to x,y,z coordinates, we have

$$\Delta \left(\frac{1}{n^2} \right)_1 = r_{13} E_z \quad (2)$$

$$\Delta \left(\frac{1}{n^2} \right)_2 = r_{13} E_z \quad (3)$$

$$\Delta \left(\frac{1}{n^2} \right)_{4,5,6} = 0 \quad (4)$$

Based on the above equations, the refractive index of the crystal due to the application of an external electric field can be calculated.

In the case of LiNbO_3 , the refractive index along the x and y directions are the same, referred to as the ordinary index, n_o . The refractive index along the z axis (or the c axis), referred to as the extraordinary index, is n_e . If we restrict the light propagating in the crystal to the TM mode, which has its E vector in the z direction, we can then neglect the effect of increase in the ordinary index, n_o . The extraordinary index due to an electric field, E_z , is given by

$$\left(\frac{1}{n_e^2}\right)_{E \neq 0} = \frac{1}{n_o^2} + r_{33} E_z \quad (5)$$

$$\left(\frac{1}{n_e^2}\right)_{E \neq 0} = \frac{1 + n_o^2 r_{33} E_z}{n_o^2} \quad (6)$$

$$(n_e)_{E \neq 0} = n_o \left(1 - \frac{1}{2} n_o^2 r_{33} E_z\right) \quad (7)$$

$$\Delta n_e = - \frac{1}{2} n_o^3 r_{33} E_z \quad (8)$$

This is the change in the refractive index in each leg of the interferometer due to an external electric field.

If V is the voltage applied to the electrodes and d is the gap between them, the electric field E_z is given by

$$E_z = \frac{V}{d} \quad (9)$$

Then,

$$\Delta n_e = - \frac{1}{2} n_o^3 r_{33} \frac{V}{d} \quad (10)$$

The phase change in the optical beam propagating in each leg of the interferometer is

$$\Delta\phi_1 = -\frac{\pi}{\lambda} n_o^3 r_{33} \frac{V}{d} L \quad (11)$$

where, λ is the wavelength of the light propagating in the waveguide.

The device configuration shown in Figure 1 operates in a push-pull fashion. The phase change associated with the second leg of the interferometer is opposite in sign to that of the first leg, i.e.,

$$\Delta\phi_2 = \frac{\pi}{\lambda} n_o^3 r_{33} \frac{V}{d} L \quad (12)$$

The total phase change is

$$|\Delta\phi_1 - \Delta\phi_2| = |\Delta\phi_c| \quad (13)$$

$$|\Delta\phi_c| = 2 \frac{\pi}{\lambda} n_o^3 r_{33} \frac{V}{d} L \quad (14)$$

The optical signal output of the interferometer is given by

$$P_s = \cos^2 \left(\frac{|\Delta\phi_c|}{2} \right) \quad (15)$$

A plot of this equation is shown in Figure 5.

The device operating point is at $\Delta\phi_c = 0$. This is a non-linear portion of the cosine squared curve. The output signal is not very sensitive to phase change at this operating point. Higher sensitivity is obtained by operating the device in the linear regime. We observe from Figure 5 that the linear portion of the curve occurs for a phase change of $\pi/2$ radian where the output signal is one half its maximum.

By operating the device at this point, the device operates in a linear fashion. Since the basic curve is a cosine squared function, linearity is maintained only over a small phase deviation. The maximum phase deviation depends on the harmonic distortion allowed in the device performance.

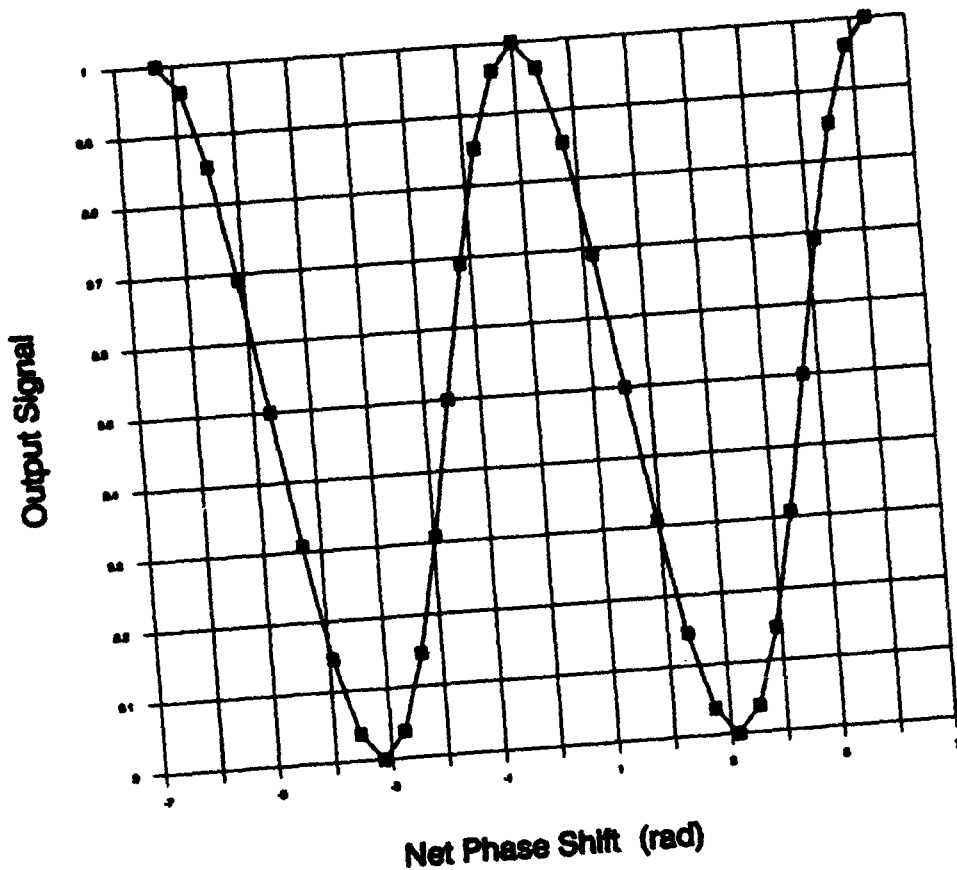


Figure 5. Output signal of a symmetric Mach-Zehnder interferometer

DOMAIN INVERSION

Ferroelectric lithium niobate exhibits spontaneous polarization below its Curie temperature, T_c . The orientation of this spontaneous polarization, P_s , can be affected, and in many situations reversed, by the application of an external electric field, a temperature gradient, a concentration gradient, or an electron beam.

While all four techniques have shown success in domain reversal in lithium niobate, it is only the concentration gradient technique that lends itself easily for applications in integrated optics. In integrated optics, selective sections of an optical circuit would require that the orientation of the spontaneous polarization be reversed compared to the bulk crystal material. This is easily accomplished by the concentration gradient effect by the mechanism of high temperature diffusion of dopants into the crystal. While elaborate schemes can be designed to apply an electric field or temperature gradient or an electron beam in selective regions of the crystal, this is quite cumbersome and does not lead to a manufacturable process.

We will provide a brief explanation of the electric field, the temperature gradient and the electron beam effects and explain in detail the effects of the concentration gradient due to doping.

ELECTRIC FIELD EFFECTS

A crystal of LiNbO_3 is heated above its Curie point. During the cooling process, an electric field of 1 V/cm is applied. When a temperature T_0 is reached, such that T_0 is slightly greater than T_c , the electric field is turned off and the crystal continues to cool to room temperature. In this situation, the crystal has a spontaneous polarization that is opposite to that of the starting material. Domain inversion is thus achieved in the crystal.

TEMPERATURE GRADIENT EFFECT

A temperature gradient of 100 C/cm across the sample thickness results in a similar effect to those observed under electric fields. When a sample is heated above its Curie temperature and cooled while maintaining a temperature gradient, the material gets poled in a sense which is related to the thermal gradient sign. If the same is now quickly heated above T_c and cooled to room temperature without any temperature gradient, the sample gets poled in a sense which is opposite to that of the starting material. We have thus achieved domain inversion in the crystal.

DOMAIN REVERSAL USING ELECTRON BEAM

This technique was published by Haycock and Townsend⁹ in 1986. It permits domain reversal on both the +C and -C surface of LiNbO₃ and LiTaO₃, at temperatures much below their Curie temperatures. This also requires simultaneous application of an electric field during the electron bombardment of the crystal.

The domain reversal was achieved in LiNbO₃, at 600 C ($T_c = 1140$ C) with an applied electric field of 10 V/cm and a beam energy of 1.8 MeV for a 1 mm thick crystal.

The domain reversal was achieved in LiTaO₃, at 400 C ($T_c = 620$ C) with an applied electric field of 900 V/cm and a beam energy of 1.8 MeV for a 1 mm thick crystal.

This approach would allow domain reversal in selected regions of a crystal to form optical waveguide circuits. This is possible since the crystal is covered by a gold film patterned by photolithography to protect the rest of the crystal from being bombarded by the electron beam. An electric field is applied to this gold electrode during the process.

While this technique offers the choice of +C and -C surfaces and a lower temperature processing, it requires access to an electron beam source. Using the e-beam process, Keys et. al.¹⁰ have created a grating structure for obtaining SHG in LiNbO₃.

CONCENTRATION GRADIENT EFFECT

Concentration gradient is created in bulk crystals by introducing dopants in the crystal growth process. For integrated optic devices, dopants are introduced into the crystal in selected waveguide regions by diffusion. Miyazawa discovered domain inversion in LiNbO₃, when Ti metal was diffused into the crystal. In particular, it is only the diffusion of Ti into the +C surface layer that resulted in domain inversion. The -C surface showed almost no domain inversion due to Ti diffusion. He was able to create both slab waveguide and stripe waveguide in the +C surface of lithium niobate. In a slab waveguide configuration, a layer of Ti is diffused on the complete surface of the crystal. In this case, light confinement is possible only in the waveguide

⁹P.W. Haycock and P.D. Townsend, "A method of poling LiNbO₃ and LiTaO₃, below T_c ", Applied Phys. Lett. **48**, pp. 698-700 (1986).

¹⁰R.W. Keys et. al., "Fabrication of domain reversed gratings for SHG in LiNbO₃, by electron beam bombardment", Electronics Lett. **26**, pp. 188-189 (1990).

thickness. In a stripe waveguide configuration, Ti is patterned to a width of a few microns and then diffused. In this case, light confinement is possible in both the lateral and vertical directions.

A simple chemical etch technique was used to reveal the domain structure in the Ti-diffused layers. A boiling solution, 110 C, of HNO₃ and HF (2:1) was used to etch the sample over three minutes.

An undiffused crystal of LiNbO₃, as received from the manufacturer will exhibit deeply etched patterns on the -C surface and scarcely etched pattern on the +C surface. After Ti diffusion, the +C surface shows deeply etched pattern. The etch pattern on the Ti diffused -C surface is no different from the original crystal surface. This indicates that the Ti diffused layer behaves in the fashion of a -C surface leading to the conclusion that a domain inversion has taken place in that region.

The crystal was wrapped in a Pt foil to suppress out diffusion of Li at high temperatures. A slab waveguide created by diffusing 500Å Ti at 1050 C for 10 hours could support three (3) modes at the wavelength of the He-Ne laser ($\lambda = 6328\text{\AA}$).

An experiment to characterize the degree of depoling (or domain inversion) was carried out by diffusing Ti at several temperatures from 950 C to 1100 C for 5 h and 10 h. Only partial depoling occurred below 1020 C. For the shorter diffusion time of 5 h, 100% depoling occurred at lower temperature compared to 10 h diffusion time. At temperatures beyond 1020 C, 100% depoling occurred for both 5 and 10 h diffusion time. The average diffusion depth was found to be 10 microns. The Ti concentration at the top surface is higher for a 5 h diffusion than for a 10 h diffusion process at the same temperature. For temperatures where 100 % depoling does not take place, it was observed that the shorter diffusion time process yields a higher degree of depoling, leading to the conclusion that the domain inversion is related to the Ti concentration.

Stripe waveguides were also created for several widths ranging from 4 to 10 μm . It was noticed that 4 and 5 μm wide guides exhibited partial domain inversion whereas guide widths of 6 - 10 μm were 100% depoled. The Ti concentration in the 4 and 5 μm wide guides are not believed to be sufficient enough to create 100% depoling. Hence, a thicker Ti layer would achieve the desired 100% domain inversion in these 4 and 5 μm guide widths.

PROCESS SEQUENCE FOR CREATING DOMAIN INVERTED REGIONS

The process requires defining Ti metal in selected regions of the substrate for subsequent diffusion operation. Standard photolithographic process techniques developed in microelectronic device technology is used for Ti pattern definition.

In the process shown in Figure 6, a layer of photoresist is spin coated on to the substrate. A photomask that has the required pattern written on it is placed on top of this substrate in a mask aligner. The photoresist is exposed to a UV light source through the photomask. When the substrate is processed in developer solution, the photoresist is etched off from regions that were exposed through the photomask. A layer of Ti, 500 Å to 1000 Å, is deposited by evaporation to cover the entire surface of the substrate. When this substrate is soaked in acetone, the photoresist is removed and thus lifts off the Ti metal that is on top of the photoresist. Ti metal is present only in regions of the substrate that had the photoresist etched in the earlier step. The substrate is cleaned and is ready for diffusion.

The diffusion process is carried out in an open tube furnace at around 1025 C. The substrate is placed on an alumina boat which is positioned in the center zone of the furnace. The furnace atmosphere is oxygen saturated with water vapor to prevent outdiffusion of titanium. Typical oxygen flow rate is around 1 to 1.5 SLM (standard liters per minute) and the water temperature is greater than 60 C.

The furnace temperature is increased gradually to the desired diffusion temperature of 1025 C over a 2 hour period so as not to thermally shock the crystal. At the end of the diffusion period, the furnace is turned off and allowed to cool to room temperature before retrieving the substrate from the furnace.

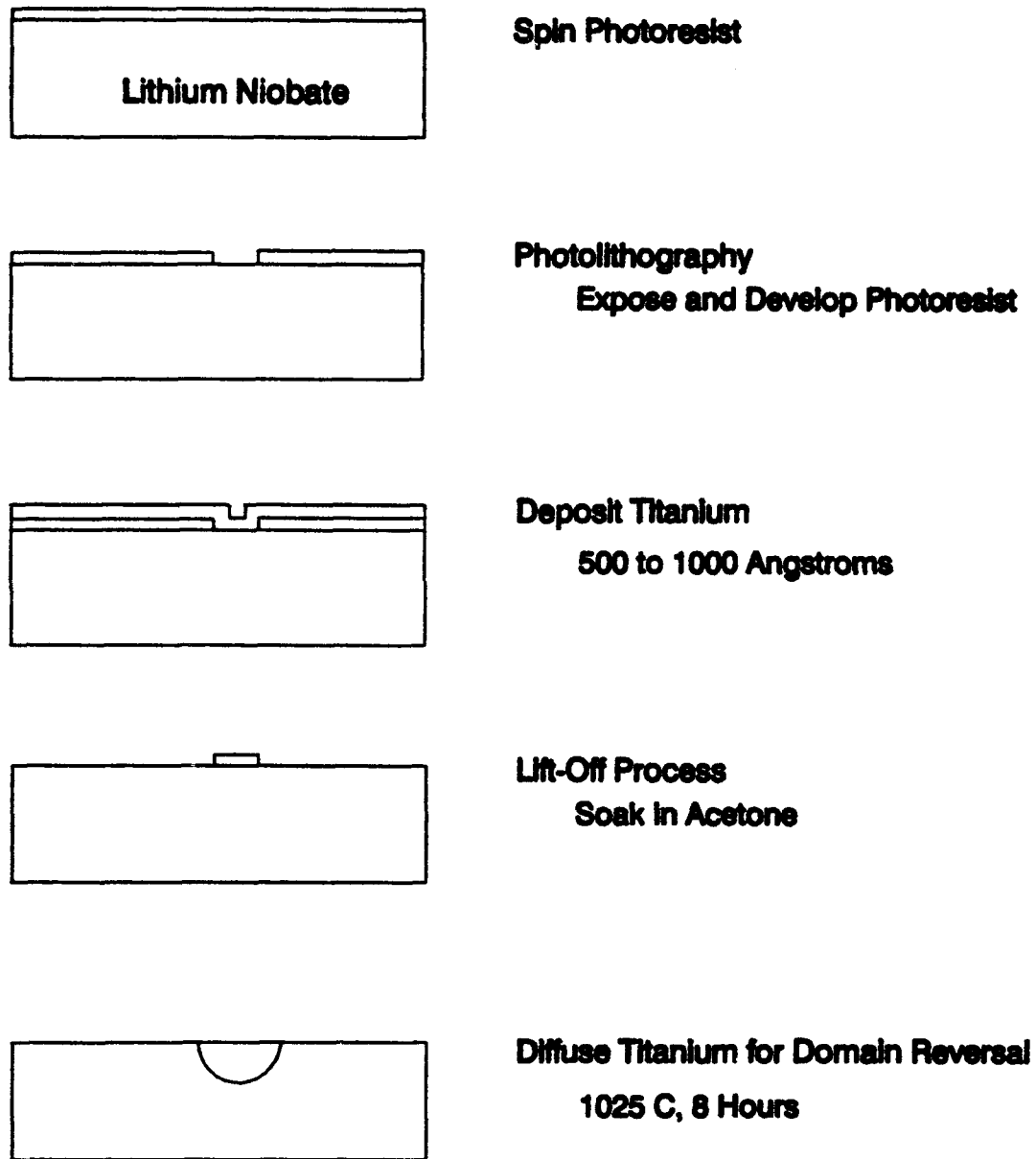


Figure 6. Process sequence for creating domain inversion in a +Z oriented lithium niobate substrate

DOMAIN INVERSION EXPERIMENTS

Feasibility experiments were carried out during the Phase I SBIR program to demonstrate selective polarization reversal in a +Z oriented LiNbO_3 substrate. The process conditions were determined to obtain 100% domain reversal in the Ti diffused regions.

The experiments to characterize the degree of depoling (or domain inversion) were carried out by diffusing Ti in LiNbO_3 at a temperature beyond 1000 C. A simple chemical etch technique was used to reveal the domain structure in the Ti-diffused layers. A solution of HNO_3 and HF (2:1) at a temperature of 80 to 90 C was used to etch the sample over three minutes.

First, a -Z oriented LiNbO_3 substrate was diffused with 1000Å of Ti at 1025 C for 8 hours. After diffusion, the crystal was etched in the above mentioned solution. The etch pits thus produced, shown in Figure 7, are typical of the -Z oriented LiNbO_3 crystal surface. We will use Figure 7 as a reference to measure the degree of domain inversion in the +Z oriented crystal.

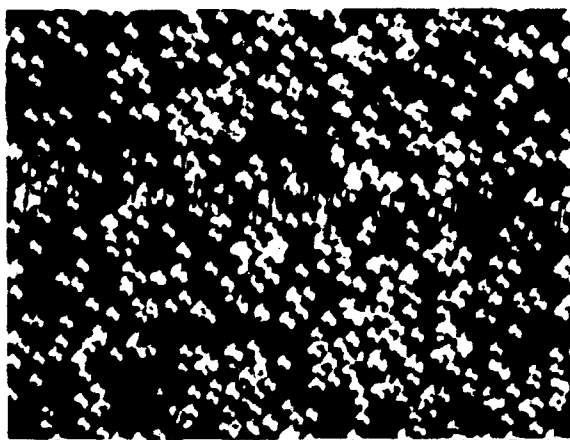


Figure 7. -Z oriented lithium niobate crystal diffused with 1000Å of titanium and subsequently etched in HF:HNO₃ at 80 to 90 C for 3 minutes

The +Z oriented LiNbO_3 is normally resistant to the acid etch solution described above. But, after Ti diffusion, the +Z surface exhibits deeply etched patterns. Figures 8 and 9 show the etch patterns of a Ti diffused +Z LiNbO_3 surface. The thickness of the Ti were 1000 and 500Å respectively and the diffusion was carried out at 1025 C for 8 hours. The etch pattern on the Ti diffused +Z surface, Figure 8, is identical to that of the -Z surface as shown in Figure 7. This indicates that the Ti diffused layer in the +Z surface behaves in the fashion of a -Z surface leading to the conclusion that a domain inversion has taken place in that region.

The degree of domain inversion is estimated from the etch pit density shown in Figures 8 and 9. Since the etch pits of Figures 7 and 8 are identical, we conclude that the diffusion of 1000Å of Ti into a +Z surface has led to a 100% domain reversal to a -Z oriented surface. The etch pits shown in Figure 9 associated with 500Å of Ti diffused into a +Z surface exhibit a much lower etch pit density compared to Figures 7 and 8, indicating only a partial domain inversion for this process condition.



Figure 8. +Z LiNbO_3 ,
1000Å Ti @ 1025 C, 8h
Etched in HF:HNO₃

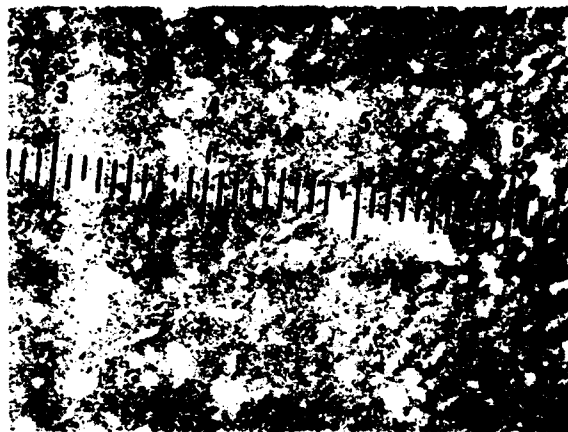


Figure 9. +Z LiNbO_3 ,
500Å Ti @ 1025 C, 8h
Etched in HF:HNO₃

The diffusion operation was also carried out at a temperature of 1050 C for 8 hours for Ti thickness of 1000Å. The higher diffusion temperature leads to further diffusion of Ti and, thus, a decrease in the concentration gradient. This reduction in the titanium concentration gradient leads to a less than 100% domain inversion. The etch pits produced in this sample after etching in HF:HNO₃ is shown in Figure 10. The etch pit density is significantly lower than that of the reference sample shown in Figure 7. The degree of depoling in this sample is estimated to be less than 50%.



Figure 10. +Z oriented lithium niobate crystal diffused with 1000Å titanium at 1050 C for 8 hours and subsequently etched in HF:HNO₃ at 80 to 90 C for 3 minutes

Titanium stripes were also created for several widths ranging from 2 to 15 μm. The thickness of the Ti was 1000Å, and the diffusion was carried out at 1025 C for 8 hours. It was noticed that widths smaller than 5 microns exhibited partial domain inversion whereas widths 6 microns and greater were 100% depoled. Figure 11 shows the etch pits produced in a 9 μm wide Ti diffused channel in a +Z oriented surface. The density of etch pits are similar to that shown in Figures 7 and 8, indicating 100% domain inversion in the Ti diffused stripe region. Also, note that the surface outside the Ti diffused region does not exhibit etch pits. The non-Ti diffused region merely exhibits scratches which is a result of the acid etch process. The cross sections of the same sample were shown in Figures 2a and 2b. The 9 μm wide stripe increases to a width of 18 μm due to lateral diffusion. Since the two legs of the Mach

Zehnder interferometer are separated by at least 50 μm , the lateral diffusion would have no effect on the device performance.

We conclude that selective 100% domain reversal is accomplished in a +Z LiNbO_3 surface by diffusing a 1000 \AA thick Ti at 1025 C for 8 hours. The width of the Ti stripe should at least be 6 microns.

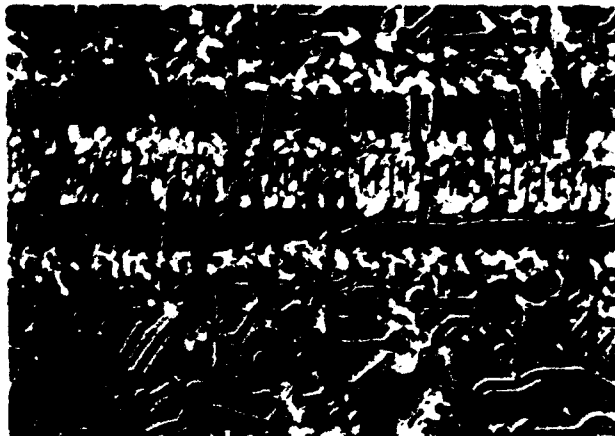


Figure 11. +Z oriented lithium niobate crystal showing 9 micron wide channel diffused with 1000 \AA titanium at 1025 C for 8 hours and subsequently etched in HF:HNO₃ at 80 to 90 C for 3 minutes

PROTON-EXCHANGE WAVEGUIDE PROCESS

The Mach-Zehnder interferometer waveguide structure is to be fabricated in a +Z oriented LiNbO_3 substrate. Selective sections of this crystal are reverse poled using the high temperature diffusion process explained earlier. One leg of the interferometer is aligned to be within this reverse poled section of the crystal.

The process of creating the waveguide structure must be such that it does not degrade the previous process performed on the crystal. There are two well established processes for fabricating waveguides in LiNbO_3 . These are high temperature diffusion of titanium and proton exchange in organic acids.

In the specific crystal orientation chosen for this device, the process of Ti diffusion leads to domain inversion for temperatures higher than 1025 C. It is reported that at 1000 C diffusion temperature, no domain inversion takes place. We could therefore fabricate waveguides at this temperature. Unfortunately, the diffusion time required would be very high, greater than 10 hours to obtain waveguides that operate at 1.3 μm wavelength. This second diffusion step would further diffuse the Ti already present in the domain inverted region and could severely degrade the waveguide performance in this region. At the end of this two-step diffusion process, the crystal would have undergone a total of 18 hours of high temperature processing - 8 hours at 1025 C and 10 hours at 1000 C. The overall substrate could be affected by such a long exposure to high temperature. For example, this could lead to excessive outdiffusion of Li from the LiNbO_3 , leading to unwanted surface guides.

The second approach to waveguide fabrication is the so called proton-exchange process. The waveguide process temperature is in the range of 200 to 400 C and would therefore not affect the Ti diffused domain inverted regions or the crystal substrate. Protons from benzoic acid exchange with Li in LiNbO_3 , to form the waveguide. This was first described by J.L. Jackel of Bell Laboratories. This is a low temperature process that allows for simple waveguide fabrication techniques. In addition, there are two other distinct advantages to using this technique.

First, the waveguide thus fabricated is truly single mode. This process only increases the extraordinary refractive index, n_e , with a slight decrease in the index of the ordinary ray, n_o . This permits only a single polarization to propagate in the waveguide which is of importance in a Mach-Zehnder interferometer, this being a polarization sensitive device. Second, the proton-exchange

waveguides exhibit higher optical damage threshold¹¹ compared to Ti diffused waveguides. Hence, this would allow greater optical power to propagate in the proton exchanged waveguide, thus resulting in greater device sensitivity.

We, therefore, select the proton-exchange process to fabricate waveguides for this Mach-Zehnder interferometer device.

The proton-exchange (PE) process in LiNbO₃ can be broadly described as the depletion of lithium ions and its replacement with hydrogen ions in the crystal. This occurs when the crystal is immersed in a protonic source such as benzoic acid.

In order to obtain optical waveguides, only a partial exchange is required. In fact, 100% exchange of H⁺ for Li⁺ leads to changes in the crystal structure and cracking of the crystal due to excessive stress.

The reaction mechanism is



Successful waveguide formation is achieved with $0.8 \geq x \geq 0$.

The exchange process is accomplished by using either pure benzoic acid or benzoic acid diluted with lithium benzoate. The process temperature is in the range of 200 to 250 C. The process time depends on the type of waveguide i.e. single or multimode and its wavelength of operation. The exchange time is typically 30 minutes to several hours, again depending on the type of waveguide required.

This PE waveguide is known to be unstable due to further migration of protons within the thickness of the guiding layer. The refractive index profile has also been observed to vary with time¹². The waveguides fabricated in pure benzoic acid exhibit increased propagation loss and scattering loss. Earlier devices fabricated by the PE process also exhibited a degradation in the electro-optic effect.

¹¹K.K. Wong, "Electro-optic frequency translators in lithium niobate fabricated by titanium indiffusion and proton exchange", Ph.D. Thesis, University of Glasgow, Glasgow, Scotland, 1989.

¹²K.K. Wong et. al., "Characterization of proton exchange slab optical waveguides in X-cut LiNbO₃", IEE Proceedings, Part J 133, pp. 113-117 (1986).

The above problems were overcome by Suchoski et. al.¹³ by performing an annealing operation after the proton-exchange process. The annealing operation was carried out in flowing oxygen at 350 C for four hours to obtain waveguides at 1.55 μm wavelength. This dramatically reduced the waveguide loss, was stable over a temperature range of 25 - 150 C, and did not exhibit any degradation in the electro-optic effect.

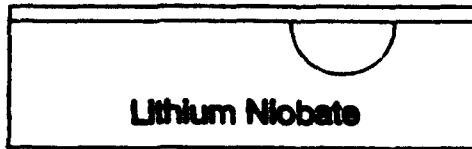
PROCESS SEQUENCE

The process sequence for an electrode-less Mach-Zehnder interferometer is shown in Figure 12. The LiNbO_3 substrate has a domain inverted Ti diffused region as shown in this figure. A thin layer of aluminum, 1000 \AA , is deposited on the surface of the crystal. Next, a layer of photoresist is coated and the waveguide pattern is defined on the photoresist using photolithography. In the photolithographic step, a photomask, which has the waveguide pattern written on it, is placed on top of the photoresist coated substrate. The photoresist is exposed, through the photomask, using a UV light source. After exposure, the substrate is developed in a developer solution. The photoresist is thus removed in areas where the waveguide is to be defined. The underlying aluminum layer is etched using photoresist as a protective layer to prevent the aluminum from etching in areas underneath the photoresist. The substrate is then immersed in a benzoic acid melt at 200 C. The proton exchange takes place only in regions where the aluminum has been etched. The aluminum layer prevents the PE process taking place underneath it. The aluminum layer is completely removed in phosphoric acid. The crystal is then annealed in flowing oxygen at 350 C for 4 hours to form the desired waveguide device.

The overall process to create an electrode-less Mach-Zehnder interferometer electric field sensor consists of a high temperature Ti diffusion process followed by a proton exchange process. A sketch of this device structure is shown in Figure 13. The proton-exchange waveguide in the lower leg of the interferometer is placed within the Ti diffused domain inverted region.

In the device shown, there is an abrupt change in the propagation constant of the optical wave as it enters and leaves the Ti diffused region. The propagation constant of the purely PE region could be different than that of the PE region within the Ti diffused region in the range of $5 \times 10^{-4} / \mu\text{m}$. This could lead to increased light scattering and loss at the junction region.

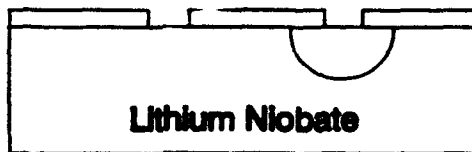
¹³P.G. Suchoski Jr., "Passive polarization/polarization maintaining components based on proton-exchanged lithium niobate", SPIE 1177, Boston, MA, 1989.



Deposit Aluminum
1000 Angstrom



Photolithography
Spin Photoresist
Expose and Develop Photoresist



Etch Aluminum
Phosphoric Acid
Strip Photoresist



Proton Exchange Waveguide
Benzoic Acid
200 C, 30 Minute
Strip Aluminum
Anneal in Oxygen
350 C, 4 Hours

Figure 12. Process sequence for creating proton-exchange waveguide in lithium niobate

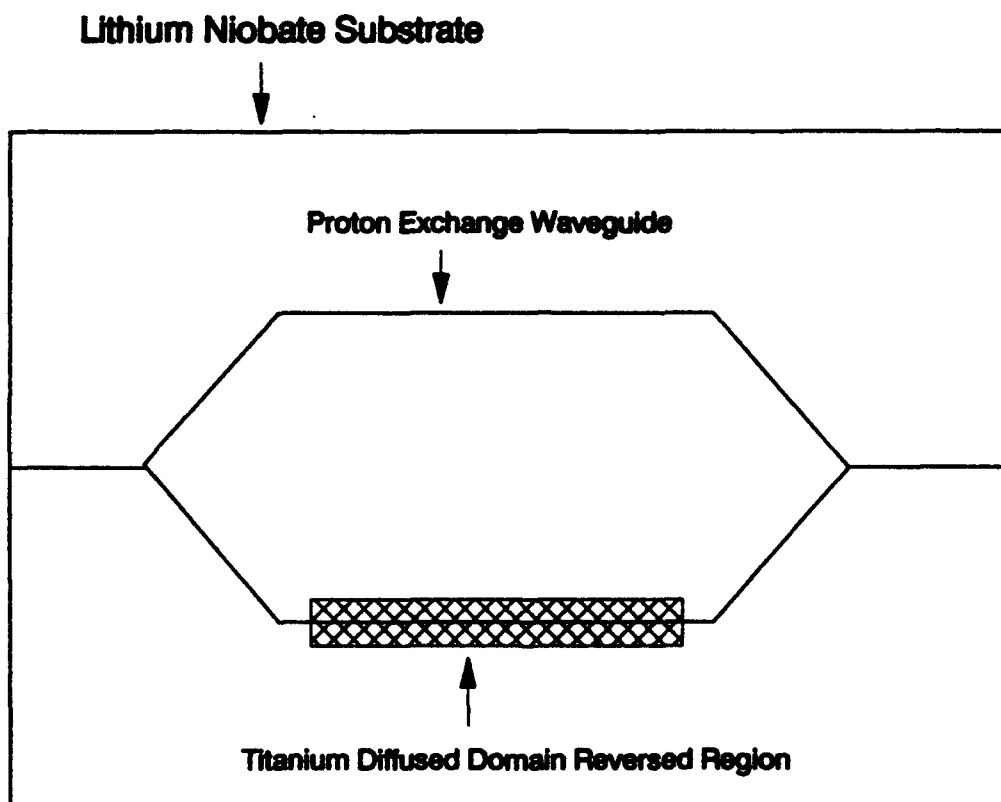


Figure 13. Schematic of an electrode-less Mach-Zehnder interferometer

A gradual change in the junction region could be obtained by modifying the width or the thickness of the Ti layer. The width or the thickness could be tapered over a length of a few hundred microns at the junction regions. It is more practical to taper the width than the thickness of the Ti layer.

For example, if the desired width of the Ti layer is $9\mu\text{m}$, the width of the Ti layer could increase from zero (in practice, less than $0.25\mu\text{m}$) to the desired width of $9\mu\text{m}$. This can be easily accomplished by incorporating the design in the photomask used to define the Ti pattern on the substrate.

Since the domain inversion effect depends on the concentration of titanium, gradual domain inversion would also occur in the transition region. A sketch of such a device that has a tapered Ti width is shown in Figure 14. If each of the transition regions required 0.5 mm , and the total length of the Ti region is 10 mm , 100% domain inversion takes place only over 9 mm length of the Ti diffused region. If we assume that the transition region contributes to only 50% domain inversion, a decrease of 5% in total phase shift occurs compared to a non-tapered design. This could be accommodated by appropriately increasing the straight segment to be equal to 9.5 mm .

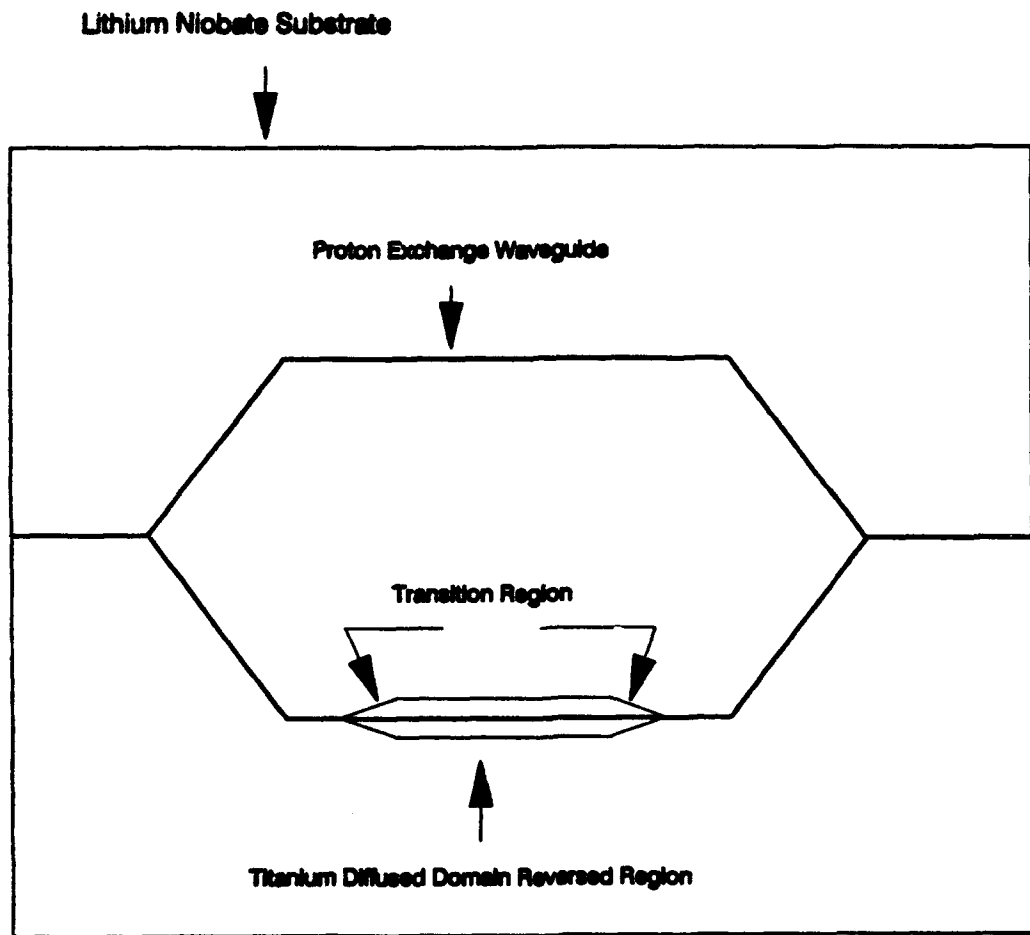


Figure 14. Schematic of a tapered Ti region to overcome the effects of abrupt steps in the lower leg of the interferometer

ELECTRODE-LESS MACH-ZEHNDER INTERFEROMETER

An electrode-less Mach-Zehnder interferometer for sensing electromagnetic fields is shown in Figure 14. The Mach-Zehnder interferometer is fabricated in an electro-optic lithium niobate crystal material. One leg of the interferometer consists of an ion-exchange waveguide within a Ti diffused domain inverted region. The other leg of the interferometer is made of an ion-exchanged waveguide. There is, therefore, a built-in asymmetry in this device leading to a phase bias in the absence of any external electric field.

When a Z-directed electric field is applied to the device, it changes the refractive index of the material through the linear electro-optic effect. The light beam experiences a phase shift as it propagates through the waveguide. Since one leg of the interferometer is oppositely poled, it experiences an equal but opposite phase shift to that of the other leg of the interferometer. This device thus operates in the same fashion as an electroded device described earlier.

QUADRATURE PHASE BIAS

The quadrature phase bias can be implemented in a Mach-Zehnder using several approaches. In the first approach, a DC bias is applied to one leg of the interferometer. The DC voltage creates a phase difference through the linear electro-optic effect. Since this requires metal electrodes to be placed on the crystal, it is not applicable in the case of a non-metallic electric field sensor.

The second approach is based on creating an optical path length difference in the device design and fabrication process. The optical path length is a product of the physical length and the effective index of the guided mode in the waveguide. Hence, a difference in the physical length or the effective index, n_{eff} , between the two legs of the interferometer could be used to create a net phase shift of $\pi/2$.

In the case where the two legs of the interferometer have lengths L_1 and L_2 and the effective index is the same, the net phase difference in the absence of any electric field is

$$|\Delta\phi_c| = \frac{2\pi}{\lambda} n_{eff} |L_1 - L_2| \quad (17)$$

or

$$|\Delta\phi_c| = \frac{2\pi}{\lambda} n_{eff} \Delta L \quad (18)$$

For a phase difference of $\pi/2$, the physical path length difference required is

$$\Delta L = \frac{\lambda}{4} \frac{1}{n_{eff}} \quad (19)$$

For $\lambda = 1.3 \mu\text{m}$ and $n_{eff} \approx 2.15$,

$$\Delta L = 0.15 \mu\text{m}.$$

Such a small path difference is difficult to fabricate using current technology of lithography and processing. Fortunately, the periodic nature of the cosine squared function associated with the MZ transfer curve can be used to implement a phase difference that is an odd multiple of $\pi/2$ or an odd multiple of ΔL , such that

$$\Delta L = m \times 0.15 \mu\text{m}.$$

The fabrication process is, therefore, relaxed by choosing a path length difference of several microns.

In the case where the $\pi/2$ phase bias is obtained by creating two different waveguide effective indices, the device is designed such that only the two straight sections have a differing n_{eff} . The input and output Y-branches have identical effective indices so that they do not contribute to any phase bias.

If the length of the straight section is L , and n_{eff1} and n_{eff2} are their effective mode indices, the net phase bias is

$$|\Delta\phi_c| = \frac{2\pi}{\lambda} L |n_{eff1} - n_{eff2}| \quad (20)$$

or

$$|\Delta\phi_c| = \frac{2\pi}{\lambda} \Delta n_{eff} \quad (21)$$

A $\pi/2$ phase bias is obtained when

$$\Delta n_{eff} = \frac{\lambda}{4L} \quad (22)$$

The branching angle at the input and output of a Mach-Zehnder interferometer is small, on the order of one degree. It is, thus, more convenient to keep the physical size of this interferometer balanced. To do this and still achieve built-in quadrature bias, we will first try to achieve the quadrature phase shift by choosing the length of the arms appropriately. The presence of Ti in one arm will lead to an inherent phase difference between the two arms.

If it is possible to choose the arm length so as to give a phase difference of an odd multiple of $\pi/2$, quadrature operation may be achieved in this way.

The quadrature bias condition for the electrode-less device under consideration could be obtained using the optical path length difference based on the difference in the effective indices of the two legs of the interferometer. The electric field sensor concept being pursued involves a Mach-Zehnder interferometer fabricated on a LiNbO₃ substrate in which one arm consists of an optical channel waveguide formed by proton-exchange and one arm formed by proton-exchange plus in-diffusion of titanium. Because both Ti diffusion and proton-exchange each cause an increase in refractive index, the interferometer is unbalanced. The object of this design is to allow the interferometer to operate with a quadrature phase shift between the two arms.

The cross section of the upper leg shown in Figure 15 consists of a proton-exchange waveguide in a LiNbO₃ substrate. This is illustrated in Figure 16 as a three layer model consisting of a lithium niobate substrate, proton-exchange waveguide and superstrate (air). The proton-exchange increases only the extraordinary refractive index of the crystal and does not affect the ordinary refractive index. Hence, the ordinary refractive index of the proton-exchange waveguide region is the same as that of the substrate.

The cross section of the lower leg shown in Figure 17 consists of a proton-exchange waveguide within the domain inverted region of the lithium niobate substrate. This is illustrated in Figure 18 as a three layer model consisting of a Ti diffused lithium niobate substrate region, proton-exchange waveguide and superstrate (air). As explained earlier, the proton-exchange process does not affect the ordinary index of the waveguide. Hence the ordinary refractive index of the waveguide region is the same as that of the Ti diffused region.

We shall now analyze the difference in effective refractive index between the two arms of the interferometer described above. We begin our analysis by considering a three layer planar structure in which the three layers are the substrate, the waveguide region and air having refractive indices n_s , n_w and n_a respectively. We assume no electromagnetic field variation in the y direction and that propagation in the z direction is described by

$$e^{i(\omega t - \beta z)} \quad (23)$$

where β is the mode propagation constant.

The electromagnetic wave equation may then be solved for the transverse electric (TE) and transverse magnetic (TM) cases. The

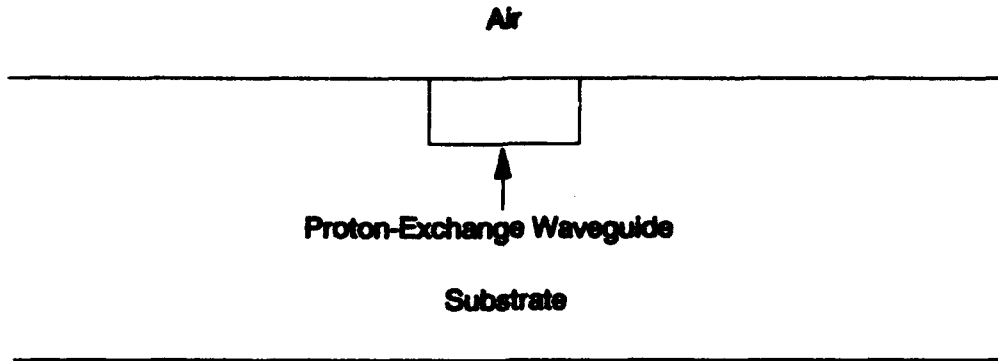


Figure 15. Cross section of the proton-exchange waveguide in the upper leg of the Mach-Zehnder interferometer

Air	$n = 1.0$
Waveguide (Proton-Exchange)	$n = 2.153$
Substrate (Lithium Niobate)	$n = 2.15$

Figure 16. Three layer model of the PE waveguide

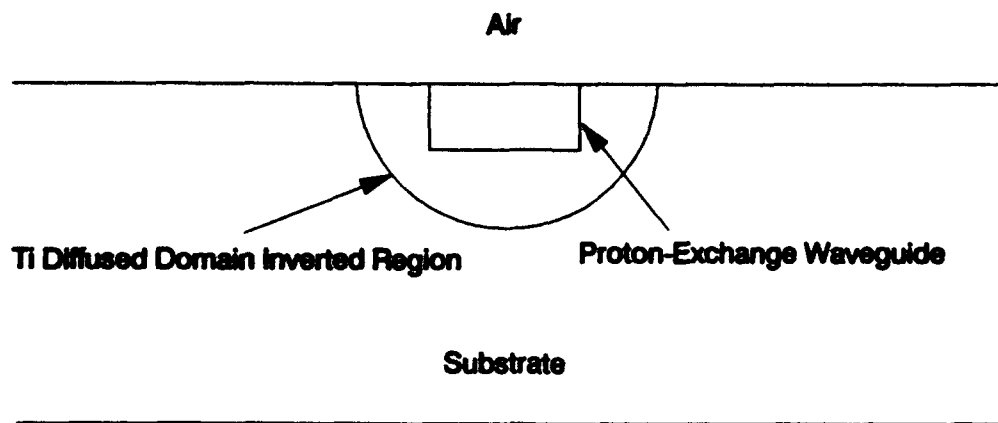


Figure 17. Cross section of the proton-exchange waveguide in the Ti diffused domain inverted region in the lower leg of the Mach-Zehnder interferometer

Air	$n = 1.0$
Waveguide (Proton-Exchange + Ti Diffusion)	$n = 2.154$
Substrate (Ti Diffusion)	$n = 2.151$

Figure 18. Three layer model of the PE/Ti waveguide

Air	$n = 1.0$
Waveguide (Proton-Exchange + Ti Diffusion)	$n = 2.154$
Ti Diffused Region	$n = 2.151$
Substrate (Lithium Niobate)	$n = 2.15$

Figure 19. Four layer model of the PE/Ti waveguide

effective refractive index is defined as

$$n_{eff} = \frac{\beta}{\kappa} \quad (24)$$

where $\kappa = 2\pi/\lambda$ and λ is the free space wavelength.

We consider solutions of the wave equation for $n_2 < n_{eff} < n_1$, assuming $n_3 > n_1$. Imposing boundary conditions and radiation conditions at $x = \pm\infty$ requires that κ for each mode must satisfy

$$\tan h\kappa = \frac{\mu}{\gamma} \quad (25)$$

for TE and TM modes, where

$$q = (\beta^2 - \kappa^2 n_1^2)^{\frac{1}{2}} \quad (26)$$

$$h = (\kappa^2 n_2^2 - \beta^2)^{\frac{1}{2}} \quad (27)$$

$$p = (\beta^2 - \kappa^2 n_3^2)^{\frac{1}{2}} \quad (28)$$

and

$$\sigma_1 = 1 \quad (TE \text{ modes}) \quad (29)$$

$$\sigma_1 = \frac{1}{n_1^2} \quad (TM \text{ modes}) \quad (30)$$

$$\gamma = \sigma_2^2 h^2 - \sigma_1 \sigma_3 p q \quad (31)$$

$$\mu = \sigma_2 h (\sigma_1 q + \sigma_3 p) \quad (32)$$

We have used the above equations to evaluate the effective refractive index, n_{eff} , for the two cases of (1) a proton-exchanged waveguide and (2) a proton-exchanged waveguide in which Ti has also been diffused. A Fortran program which uses double precision has been used to make this calculation. We have considered single mode

waveguides and the TM polarization for the planar waveguide. We have made realistic assumptions that the presence of Ti causes the refractive index to increase by 0.001 and that the proton-exchange process leads to a refractive index increase of 0.003 for the TM mode. In this calculation we assume that the Ti diffusion is sufficiently deep so that the diffused region can act as the substrate. Later, we determine the depth for which this assumption is valid. The parameters used and the results of the calculation are listed in Table III. The change in effective index due to the presence of Ti is 0.001001 or just 0.001, the same value as the actual refractive index change we assumed. This same result has been obtained for a range of parameters, that is, the change in effective index is equal to the change in actual index.

The change in phase $\Delta\phi$ due to the above change in effective index Δn_{eff} for a Mach-Zehnder interferometer arm length L is given as

$$\Delta\phi = \frac{2\pi}{\lambda} L \Delta n_{eff} \quad (33)$$

Quadrature operation implies that this phase shift is

$$\Delta\phi = m \frac{\pi}{2} \quad m = 1, 3, 5, \dots \quad (34)$$

This can be accomplished for lengths L given as

$$L = m \frac{\lambda}{4 \Delta n_{eff}} \quad (35)$$

Using $\Delta n_{eff} = 0.001$ from above and $\lambda = 1.3 \mu\text{m}$, we find

$$L = m \times 324.7 \quad \text{micron} \quad m = 1, 3, 5, \dots$$

This is a small enough value for $m = 1$ that achieving an odd multiple of it is realistic. The only question is the accuracy of the above calculation.

We can improve our model by using a 4-layer planar formulation on the interferometer arm which has undergone both proton-exchange and Ti diffusion. By considering an extra layer we can examine the effect of varying the depth of the Ti diffusion has on n_{eff} . For the 3-layer calculation above, we assumed that this depth was sufficiently deep for the Ti diffused layer to act as the substrate. The waveguide parameters for the 4-layer formulation are shown in Figure 19.

The thickness of the waveguide is t and the depth of the Ti diffused region is d, with the difference δ given as

Table III

3-Layer Calculation of Effective Indices

	Case 1 Proton Exchange (PE)	Case 2 PE + Ti-Indiffusion
n_{air}	1.0	1.0
n_{guide}	2.153	2.154
$n_{substrate}$	2.150	2.151
t (μm)	7.75	7.75
λ (μm)	1.3	1.3
$t_{single\ mode}$ (μm)	8.56	8.56
$n_{e\ planar}$	2.151960	2.152961

$$\delta = d - t \quad (36)$$

The effective index, β , for the above 4-layer structure is given as

$$(\sigma_1 q + \sigma_0 r) (\mu - \gamma \tan ht) + (\sigma_0 r - \sigma_1 q) e^{-2\alpha\delta} x$$

$$[(\sigma_2^2 h^2 + \sigma_1 \sigma_3 p q) \tanh t + \sigma_2 h (\sigma_1 q - \sigma_3 p)] = 0 \quad (36)$$

with the mode parameters defined in Equations (25) - (31) and

$$\gamma = (\beta^2 - \kappa^2 n_0^2)^{\frac{1}{2}} \quad (37)$$

We have calculated the effective refractive index $n_{eff}(\delta)$ as a function of δ , defined in Eq. (35). If $\delta = 0$, then the Ti depth is the same as the proton-exchange depth. As δ increases, $n_{eff}(\delta)$ also increases. For convenience, we plot this increase relative to the value of n_{eff} at $\delta = 0$ in Figure 20. Note that this difference increases with δ initially, but that it saturates once $\delta \approx 2 \mu\text{m}$. Figure 12 provides two important pieces of information: (1) the value of δ for which the difference saturates, and (2) the value of this difference at saturation. Although the actual index difference at saturation is small, $\approx 6 \times 10^{-5}$, the corresponding phase shift for a 10 mm long interaction length is

$$\delta\phi = \frac{2\pi}{\lambda} L \delta n_{eff} = \frac{2\pi}{1.3} (10 \times 10^3)(6.0 \times 10^{-5}) \approx 0.9 \pi \quad (38)$$

which, of course, is significant. In the above equation, δn_{eff} represents the change in effective index, plotted in Figure 12, in the lower leg of the interferometer due to finite δ . Thus, if δ varies between zero and the value for which the change in Figure 20 saturates, $\approx 2 \mu\text{m}$ in this example, it will have a significant effect on determining the quadrature condition. Because the exact value of δ may be hard to determine or hard to control, the best procedure may be to insure that the Ti diffusion depth is sufficiently large so that the change in effective index δn_{eff} shown in Figure 20 has saturated. For this example, the Ti diffusion depth would need to be at least $2 \mu\text{m}$ greater than the proton-exchange depth.

We can refine the calculations for the example considered above by including the effect of the channel waveguide. The simplest way to do this is to use the effective index method. To make this calculation, it is assumed that the Ti diffused region is much wider than the proton-exchange region. The results of calculating the channel waveguide effective index are presented below in Table IV. Note that although the effective indices are different

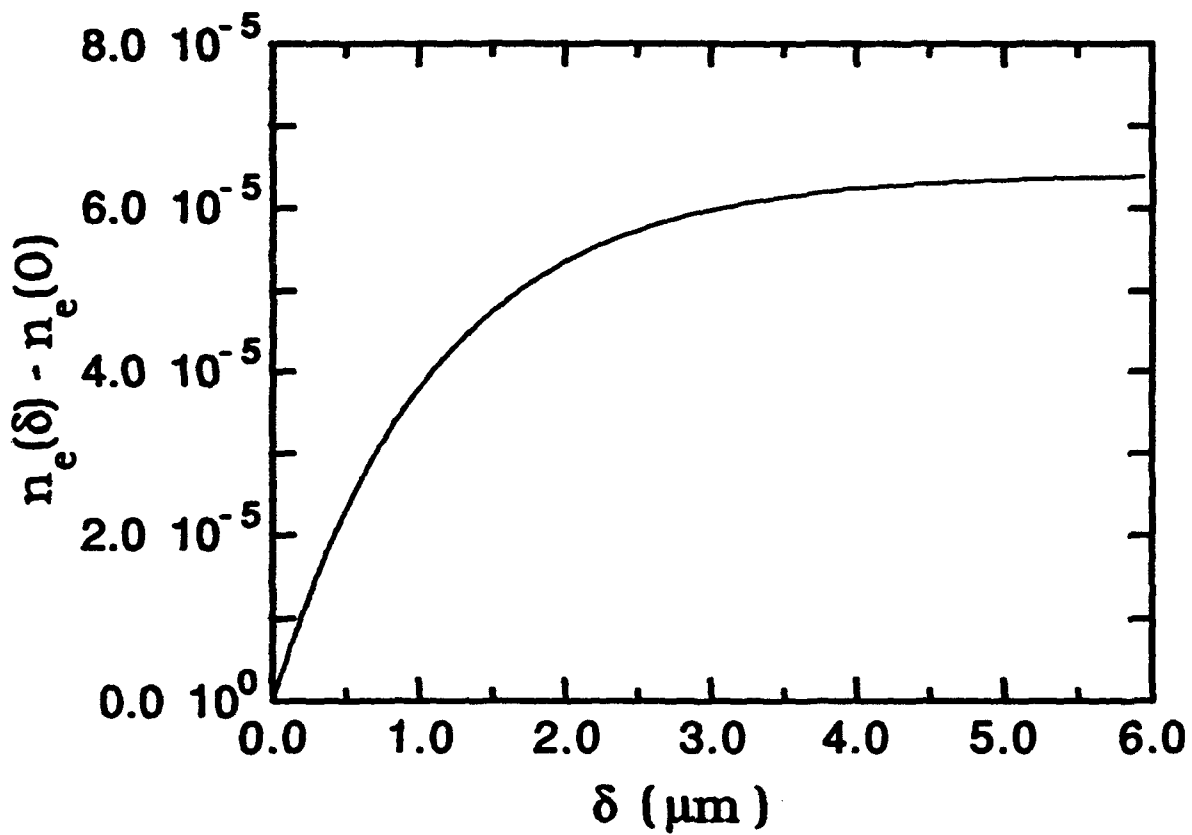


Figure 20. Plot of the effective index as a function of δ , relative to the value for $\delta = 0$

Table IV

**Effective Index Calculation of Channel
Waveguide Effective Indices**

	Case 1 Proton Exchange (PE)	Case 2 PE + Ti-Indiffusion
$n_{e \text{ planar}}$	2.151960	2.152961
n_{clad}	2.150	2.151
$w \text{ } (\mu\text{m})$	7.0	7.0
$\lambda \text{ } (\mu\text{m})$	1.3	1.3
$w_{\text{single mode}} \text{ } (\mu\text{m})$	7.08	7.08
n_e	2.151259	2.152260

than those calculated in Table III, the difference in effective indices is the same. This implies that the value of length calculated from Eq. (34) needed to achieve quadrature offset would be the same as determined earlier, that is

$$L = n \times 324.7 \text{ } \mu\text{m} \quad n = 1, 3, 5, \dots$$

This value would be modified by 4-layer considerations, as discussed earlier.

These calculations show that it may be possible to choose the quadrature point of operation by appropriately choosing length. We could improve this possibility by repeating the above calculations for actual graded index profiles, assuming we could predict the proton-exchange and Ti diffused index profiles accurately. Because small effects, such as the 4-layer effect discussed earlier, can significantly alter the quadrature point, it may still be difficult in practice to theoretically predict the quadrature point, even if elaborate graded index approaches were used. What is needed is some way to adjust the quadrature point once a device has been fabricated.

Tuning the source wavelength may be one such way to adjust the phase difference between the two arms of the interferometer. We consider such a possibility for the parameters given in Table III and for an interaction length of 10 mm. We see in Figure 21 that the difference in the effective indices of the two arms of the interferometer is nearly constant with wavelength. Although the effective index in each arm varies with wavelength, the variations in each arm are similar so that the difference remains constant. However, we see in Figure 13 that significant phase change occurs. This phase change is due to the $2\pi/\lambda$ term in Eq. (32). For the range of wavelengths considered in Figure 13 the phase change is more than sufficient ($\pm\pi/2$) to choose a value of wavelength for quadrature operation. The calculation in Figure 13 is for $L = 10$ mm; for longer lengths the range of wavelengths would be smaller. Specifically, to achieve a phase variation of $\pm\pi/2$, the range of wavelength over which the source must be tuned is

$$|\Delta\lambda| = \frac{\lambda^2}{2L\Delta n_{eff}} \quad (39)$$

measured in fractions of micron. For example, if $L = 20$ mm, $\Delta n_{eff} = .001$ and $\lambda = 1.3$ mm, then the range of wavelength over which the source needs to be tuned is $0.034 \text{ } \mu\text{m}$ to allow variation of the phase by $\pm\pi/2$, thus assuring quadrature operation can be achieved.

The discussion here has been directed at establishing a basis for designing the asymmetric Mach-Zehnder interferometer so that quadrature phase difference between light emerging from the two arms can be achieved. Numbers used here are representative of the

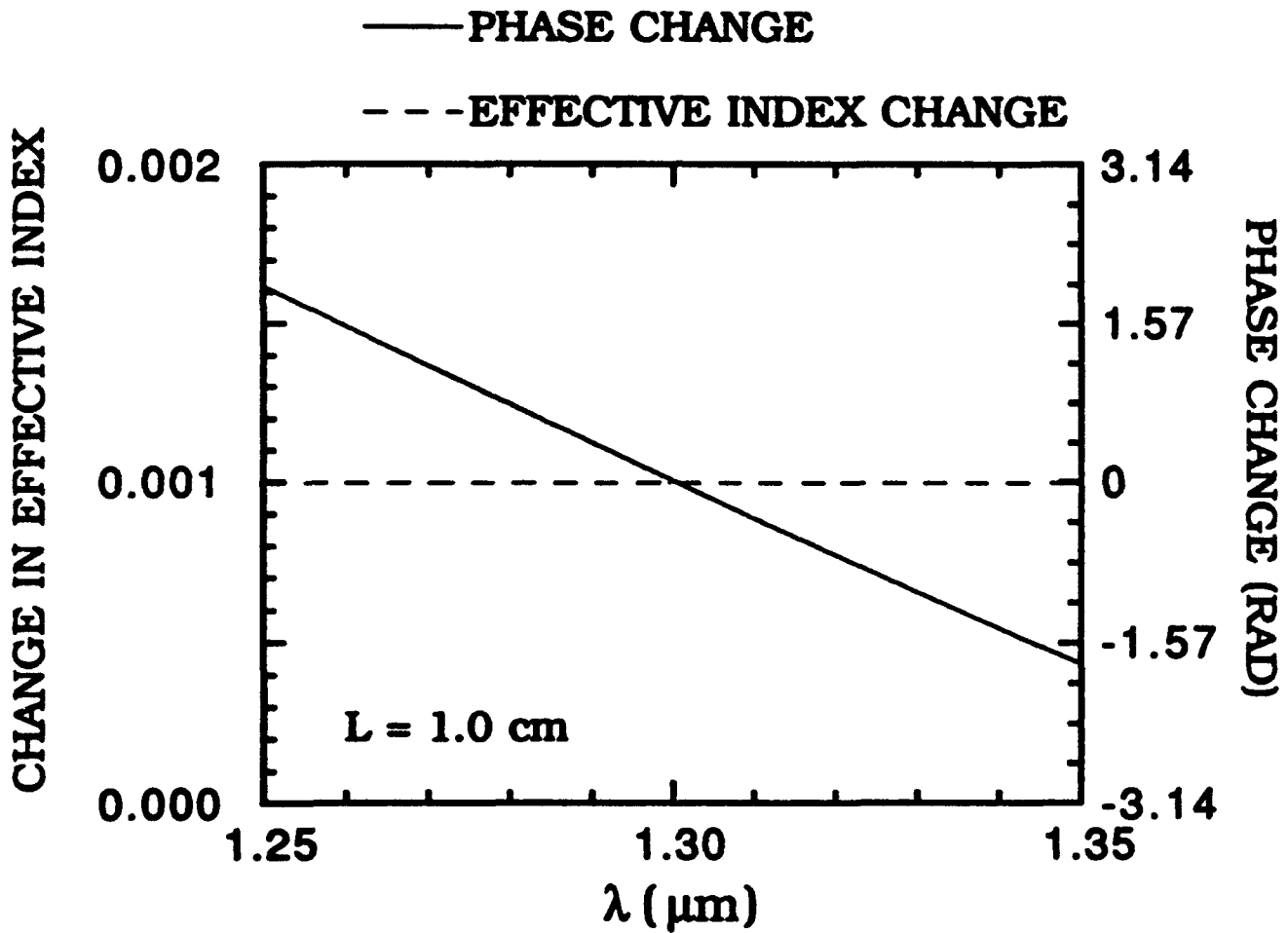


Figure 21. Plot of the change in effective index between the two arms of the interferometer and the interferometer phase change as a function of wavelength over a limited range

technologies, and results of the calculations presented here provide a basis for actual design. Planar 3-layer and 4-layer and channel optical waveguide dispersion calculations have been performed. These calculations predict a length for quadrature operation which could be achieved in practice, but these calculated lengths are sensitive to the refractive index variations associated with the proton-exchange and Ti diffusion technologies. Although more sophisticated models could be utilized, it is expected that their use would still result in the same problem. We thus have investigated the possibility of using wavelength tuning to adjust the phase difference for quadrature operation. The range of wavelength tuning required is shown to be realistic.

Another approach is to modify the depth of the proton-exchange waveguide within the Ti diffused region. The effective index is a sensitive function of δ as shown in Figure 20. We could use this property of the waveguide to tailor the bias condition using post-processing techniques. Since the proton-exchange waveguide could be driven deeper at a relatively low temperature of 200 to 400 C, a strip heater could be used to heat the device to change the bias condition. The device output could be monitored during the heating process and the heater turned off once the quadrature bias condition is reached. This could be implemented during the final testing and packaging stages of the sensor.

LASER WAVELENGTH

LiNbO₃ is transparent from the visible (0.45 μm) to the mid-infrared (4 μm). In principle, the device could operate anywhere in the transmission spectrum of the crystal. The device under consideration is based on integrated optical technology which requires single mode optical fibers for optical input and output. Single mode optical fibers are commercially available for operation in the near infrared wavelength range, we are limited to operating this device within this wavelength band. The wavelength range is divided into two bands -- 0.8 to 0.9 μm, the short wavelength region, and 1.2 to 1.6 μm, the long wavelength region. Excellent, high quality, solid state laser diodes are also commercially available at these wavelengths.

Because, as will later be seen, several milliwatts of optical power may have to be used to achieve the desired dynamic range, a wavelength of 1300 nm instead of 850 nm is preferred, so as to reduce or eliminate optical damage effects in LiNbO₃.

The selection of wavelength of operation is based on the following considerations:

- Device sensitivity
- Optical power damage threshold
- Device fabrication and packaging

DEVICE SENSITIVITY

The total phase shift in a Mach-Zehnder interferometer is given by

$$|\Delta\phi_c| = 2 \frac{\pi}{\lambda} n_o^3 r_{33} \frac{V}{d} L \quad (40)$$

The phase shift is inversely proportional to the wavelength and directly proportional to the cube of the refractive index. In general, the variation of refractive index with wavelength is very small and we can thus conclude that the total phase shift decreases as wavelength increases. The signal to noise ratio (SNR), hence the device sensitivity, is proportional to the square of the phase shift.

The improvement in device sensitivity for a device operating at 0.8 μm and 1.3 μm is given by

$$\left(\frac{\Delta\phi_{0.8}}{\Delta\phi_{1.3}} \right)^2 = \left(\frac{n_o^3}{\lambda} \right)_{0.8}^2 \left(\frac{\lambda}{n_o^3} \right)_{1.3}^2 \quad (41)$$

For $\lambda = 0.8 \mu\text{m}$, $n_o = 2.17$, and $\lambda = 1.3 \mu\text{m}$, $n_o = 2.15$,

$$\left(\frac{\Delta\phi_{0.8}}{\Delta\phi_{1.3}} \right)^2 = 2.8 = 4.5\text{dB} \quad (42)$$

We see that a device operating at $0.8 \mu\text{m}$ would give an improvement in device sensitivity of 4.5 dB based on the above calculations. This is based on the assumption that the device is capable of carrying the same amount of optical power at both these wavelengths. This is not true in LiNbO₃, due to optical power damage constraints.

OPTICAL POWER DAMAGE THRESHOLD

Optical damage is also known as photorefractive effect where the refractive index of the material is dependent on the intensity of the optical beam. The optical power density at which the material exhibits this effect is known as the threshold of optical damage.

Optical damage occurs in a LiNbO₃ crystal because of the presence of impurities. The crystal received from the manufacturer has less than a few ppm of iron and other rare earth ions. Additional impurities are introduced into the crystal during the device fabrication process. For example, the Ti metal used in diffusion carries with it additional iron impurities such that a diffused region of the substrate could have tens of ppm of iron present.

The effect of an optical beam in the crystal is to ionize impurities such as iron. The optical field in the crystal separates the free carriers from the impurities and traps these carriers in unilluminated regions resulting in a local electric field. This local field changes the refractive index in that region through the linear electro-optic effect and alters the waveguide characteristics of the crystal. The overall effect is that the optical wave initially confined in the waveguiding region is radiated into the substrate. The extent of optical damage is dependent on the power density and the wavelength of the optical signal in the waveguide. Optical power damage is significant at lower wavelengths such as $0.8 \mu\text{m}$ compared to $1.3 \mu\text{m}$.

The optical waveguide in LiNbO₃ is capable of handling 10 to 100 μW of optical power at the wavelength of $0.8 \mu\text{m}$ and greater than 10 mW of optical power at $1.3 \mu\text{m}$ wavelength. To obtain the required device sensitivity, we would require to propagate several milliwatts of optical power in each waveguide channel. Based on the optical damage considerations, we conclude that the wavelength of operation should be $1.3 \mu\text{m}$. The Mach-Zehnder device optimized to operate at $1.3 \mu\text{m}$ could also be operated at $1.55 \mu\text{m}$ wavelength.

This would provide increased optical power handling capability in the waveguide but a decreased sensitivity of 1.5 dB.

DEVICE FABRICATION AND PACKAGING

The waveguide linewidth at 1.3 μm and 0.8 μm wavelengths are 7 μm and 4 μm respectively. The larger linewidth makes the task of device fabrication easier at 1.3 μm and also increases the production yield. Similarly, the mode size of the optical waveguide and the fiber core size are larger at 1.3 μm wavelength. The alignment accuracy between an optical fiber and the device at 0.8 μm is in the submicron range. A misalignment of 0.5 μm reduces the optical coupling efficiency between the fiber and the waveguide by 3 dB. The waveguide device at 1.3 μm is extremely tolerant to misalignment of at least 3 μm before exhibiting a 3 dB optical coupling loss.

Based on these considerations, the wavelength of operation is chosen to be 1.3 μm .

SYSTEM ANALYSIS

This section provides an analysis of the proposed optical sensor system. The design of the electric field sensor is influenced by the interrelationship of several system parameters. The carrier-to-noise-ratio (CNR) for a given received optical power must first be determined. From this, the signal-to-noise-ratio (SNR) for a given peak phase modulation index is derived. This peak phase modulation index limits the dynamic range and is based on linearity considerations. The minimum detectable electric field is calculated based on SNR=1. The maximum detectable electric field is then calculated using the device geometry and the crystal properties. The minimum and maximum electric field yield the dynamic range. The results of these calculations are summarized in a tabular form at the end of this section.

CNR ANALYSIS

The carrier-to-noise-ratio (CNR) in a single-ended homodyne detection optical system is given by the following relationship:

$$\text{CNR} = \frac{2 \left(\frac{\eta e P_s M}{h f_c} \right)^2}{\left[e \left(\frac{2 \eta e P_s}{h f_c} + I_d \right) M^{(2+x)} + \frac{2 k T F}{R_L} \right] B_n} \quad (43)$$

where

- P_s = received optical power in each beam as if acting alone,
- η = quantum efficiency,
- h = Planck's constant (6.63×10^{-34} J.s),
- f_c = optical carrier frequency (2.31×10^{14} Hz for a 1300 nm source),
- I_d = dark current,
- M = avalanche gain (= 1 for a PIN photodiode),
- x = excess noise factor (= 0 for a PIN photodiode),
- k = Boltzmann's constant (1.38×10^{-23} J/K),
- F = noise figure of amplifier,
- R_L = effective load resistance,
- B_n = noise equivalent bandwidth (1.57 GHz for B_n equal to a 1 GHz signal system bandwidth).

In a system where a single pole low pass filter defines the overall bandwidth, the noise equivalent bandwidth is $\pi/2$ times the -3dB system bandwidth.

Substituting the values of $P_s = 1$ mW, $\eta = 0.67$ for a PIN diode into the above equation,

$$\text{CNR} = 63.9 \text{ dB.}$$

In the Equation (43), the CNR increases when the optical power, P_o , increases or when the bandwidth, B_n , decreases. Increasing the load resistor, R_L , will decrease the thermal noise, but it will lower the frequency response. Moreover, it will render the detector unable to detect high frequency signals. The avalanche multiplication factor M tends to increase the CNR, particularly when the optical power is very low and the thermal noise is dominant. The multiplication factor (M) for a PIN diode is 1, while that for an APD is typically between 10 and 100.

To maximize the sensitivity and dynamic range, the optical receiver is designed to be shot noise limited. The shot noise or the kT noise at 300 K is -174 dBm/Hz. If the effective photodetector load was 50 ohms, and the following amplifiers were essentially noiseless, i.e., noise figure $F = 1$, then the power reaching the photodetector would have to be sufficient to ensure that the shot noise generated in the load would be > -174 dBm/Hz. Anything less than that would limit the CNR to a value less than optimum. By using a transimpedance amplifier with a PIN photodetector, the load can be increased to about 1K ohm without compromising bandwidth. Thus, it reduces the power needed to reach the quantum noise limit.

The required dynamic range is 40 dB, corresponding to phase and electrical field ratios of 100:1. This would be adequate for sufficiently large phase modulation. In most cases, the peak phase modulation $\Delta\phi$ may have to be considerably less than unity in order to ensure a low level of distortion from the phase detector. The SNR could fall below 40 dB in such situations.

The optical source could also degrade the SNR due to excess intensity noise. This general broadband excess noise level is commonly expressed as the Relative Intensity Noise (RIN). The RIN generally has a fairly flat spectrum, except at (a) frequencies determined by external cavity resonances due to reflections back into the laser diode, (b) near the laser relaxation frequency and (c) near zero hertz. Since excess noise normally varies substantially with optical feedback, the use of an optical isolator is recommended. Optical isolators are more compact and less expensive at 1300 nm than at 800 nm wavelength.

As a rule of thumb, in a direct detection system a shot noise limited 1 mW near infrared optical system will produce a CNR of approximately 150 dBc/Hz (dBs with respect to the carrier in a 1 Hz bandwidth). This assumes that there is no excess noise. If the RIN value for this device is -140 dBc/Hz, so that the CNR saturates at high power levels to a value of 140 dB/Hz, then the excess intensity noise is about 10 dB. The dynamic range of a system using this device will, therefore, be degraded by about 10 dB.

In the following pages are included Tables V and VI generated from the Optoelectronic Spreadsheet Template CNR.WR1 developed by

CARRIER-TO-NOISE RATIOS (CNR) IN OPTICAL SYSTEMS		SYNOPSIS VERSION (CNR V1.0)			
COPYRIGHT (C) 1990 FIBERPHONE OPTOELECTRONICS Serial # SPECIAL		File Name: CNR_V01		Last Exec: 00-Dec-80	
		Project Name: ELECTRIC-FIELD SENSOR		00:57 PM	
		Sequence: 01			
TYPE OF SYSTEM		RANGE_A Data	RANGE_B Data	RANGE_C Data	RANGE_D Data
ENTER: →		3: Heterodyne	3: Heterodyne	3: Heterodyne	3: Heterodyne
1: Direct Detection Ps →		3	3	3	3
2: Heterodyne Detection Ps →					
3: Heterodyne Detection Ps →					
4: Heterodyne Detection Ps →					
5: Heterodyne Detection Ps →					
SOURCE PARAMETERS					
ENTER: →		4	4	4	4
Device Manufacturer		INGRAS LASER	INGRAS LASER	INGRAS LASER	INGRAS LASER
Type		NEC	NEC	NEC	NEC
Wavelength (W, um)		NDL30004	NDL30004	NDL30004	NDL30004
Cable Radius (R, um)		1.30	1.30	1.30	1.30
Single Longitudinal mode (Y/N)		YES	YES	YES	YES
Single Transverse mode (Y/N)		NO	NO	NO	NO
Rated Output Power (P, mW)		0.00	0.00	0.00	0.00
Threshold Current (I, mA)		20.00	20.00	20.00	20.00
Forward Current (I, mA)		20.00	20.00	20.00	20.00
Rise Time (T, ns)		1.00	1.00	1.00	1.00
Relative Intensity Noise (RIN, dB/Hz)		-100.00	-100.00	-100.00	-100.00
Linearity (L, dB)		20.00	20.00	20.00	20.00
Spectral Width (W, nm)		4.00	4.00	4.00	4.00
Vert. X Hor. Angle (Deg. X Deg.)		35 X 35	35 X 35	35 X 35	35 X 35
Coherence Length (LC, m)		5.07E+00	5.07E+00	5.07E+00	5.07E+00
TYPE OF PHOTODETECTOR		Single-Ended	Single-Ended	Single-Ended	Single-Ended
ENTER: →		1	1	1	1
1: Single-Ended					
2: Dual-Balanced					
Excess Noise Suppression (Exs, dB)		30.0	30.0	30.0	30.0
PHOTODETECTOR PARAMETERS					
ENTER: →		0	0	0	0
Manufacturer		INGRASP PIN	INGRASP PIN	INGRASP PIN	INGRASP PIN
Type		Hitachi	Hitachi	Hitachi	Hitachi
Wavelength (W, um)		MT101	MT101	MT101	MT101
Quantum Efficiency (Eta)		1.30	1.30	1.30	1.30
Avalanche Gain (G)		0.07	0.07	0.07	0.07
Excess Noise Factor (N)		0.00	0.00	0.00	0.00
Surface Leakage Current (I, nA)		0.00	0.00	0.00	0.00
Dark Current (I, nA)		7.00	7.00	7.00	7.00
Temperature (T, K)		300.00	300.00	300.00	300.00
Capacitance (C, pF)		2.00	2.00	2.00	2.00
Gain-Bandwidth (GB, GHz)		1.00	1.00	1.00	1.00
Characterization Voltage (V, Volts)		10.00	10.00	10.00	10.00
Maximum Forward Current (I, mA)		1.00	1.00	1.00	1.00
Area (A, mm^2)		0.01	0.01	0.01	0.01
FRONT-END PARAMETERS					
ENTER: →		0.0	0.0	0.0	0.0
Noise Figure (F, dB)		1000.0	1000.0	1000.0	1000.0
Load Impedance (Z, Ohm)		2.00	2.00	2.00	2.00
Silly Capacitance (C, pF)		30.0	30.0	30.0	30.0
Transimpedance Gain (AV, Ohm)		1.00E+00	1.00E+00	1.00E+00	1.00E+00
System Bandwidth (BW, Hz)		10.0	10.0	10.0	10.0
Maximum Received Power (Pr, dBm)		0.00E+00	0.00E+00	0.00E+00	0.00E+00
Background Radiation (Pb, W)					
Responsivity (R, mA/W)		7.0E-01	7.0E-01	7.0E-01	7.0E-01
Dark Current Noise (I, nA/rtz)		4.7E-02	4.7E-02	4.7E-02	4.7E-02
Thermal Current Noise (I, nA/rtz)		3.7E+00	3.7E+00	3.7E+00	3.7E+00
Noise Equivalent Power (NEP, W/rtz)		6.0E-14	6.0E-14	6.0E-14	6.0E-14
Photon Rate (Np, /s)		4.4E+03	4.4E+03	4.4E+03	4.4E+03
Bandwidth (B, Hz)		1.3E+03	1.3E+03	1.3E+03	1.3E+03
COHERENT FRONT-END PARAMETERS					
ENTER: →		0.00E+00	0.00E+00	0.00E+00	0.00E+00
Local Oscillator Power (P, W)		1.00	1.00	1.00	1.00
Mixing Efficiency (M)		0.00	0.00	0.00	0.00
Autocorrelation Length (L, m)					
Autocorrelation (R(t))		1.0E+00	1.0E+00	1.0E+00	1.0E+00
Received Optical Power Ps, dBm		CNR, dB	CNR, dB	CNR, dB	CNR, dB
-30	12.7	12.7	12.7	12.7	12.7
-29	14.7	14.7	14.7	14.7	14.7
-28	16.7	16.7	16.7	16.7	16.7
-27	18.7	18.7	18.7	18.7	18.7
-26	20.7	20.7	20.7	20.7	20.7
-25	22.7	22.7	22.7	22.7	22.7
-24	24.7	24.7	24.7	24.7	24.7
-23	26.6	26.6	26.6	26.6	26.6
-22	28.6	28.6	28.6	28.6	28.6
-21	30.6	30.3	30.3	30.3	30.3
-20	32.6	32.3	32.3	32.3	32.3
-19	34.4	34.4	34.4	34.4	34.4
-18	36.3	36.3	36.3	36.3	36.3
-17	38.2	38.2	38.2	38.0	38.0
-16	40.1	40.1	40.1	39.8	39.8
-15	41.9	41.9	41.9	41.4	41.4
-14	43.7	43.7	43.7	43.0	43.0
-13	45.5	45.5	45.5	44.4	44.4
-12	47.2	47.2	47.1	45.7	45.7
-11	48.9	48.9	48.6	46.0	46.0
-10	50.9	50.9	50.2	47.0	47.0
-9	52.1	52.0	51.6	48.5	48.5
-8	53.6	53.5	52.9	49.1	49.1
-7	55.1	54.9	54.1	49.6	49.6
-6	56.9	56.3	55.2	49.9	49.9
-5	58.9	58.8	58.0	50.4	50.4
-4	60.3	60.0	57.7	50.6	50.6
-3	61.9	61.1	58.3	50.7	50.7
-2	63.5	62.1	58.8	50.8	50.8
-1	65.0	63.9	59.2	50.9	50.9
0	65.0	64.0	59.6	50.9	50.9
1	66.1	64.9	59.9	50.9	50.9
2	67.1	65.7	60.1	50.9	50.9
3	67.1	65.7	60.1	51.0	51.0
4	68.2	66.4	60.3	51.0	51.0
5	69.2	67.0	60.3	51.0	51.0
6	70.3	67.5	60.6	51.0	51.0
7	71.3	68.2	60.7	51.0	51.0
8	72.4	68.6	60.7	51.0	51.0
9	73.4	69.0	60.8	51.0	51.0
10	74.4	69.4	60.9	51.0	51.0

Ps is the power in each beam reaching the photodetector. Since there is only one photodetector in this single-ended system, the total power into the Mach-Zehnder Electric-Field Sensor must be at least 4Ps. Thus, the performance at 0 dBm corresponds to a minimum input power of 4 mW.

Table V -- CNR for single-ended detection

CARRIER-TO-NOISE RATIO (CNR) IN OPTICAL SYSTEMS		PROGRAM VERSION (CNR 001 V1.0)			
COPYRIGHT (C) 1980 FIBERLINE OPTOELECTRONICS Serial # SPECIAL		Last Calc: 06-28-80 08:55:28			
TYPE OF SYSTEM		RANGE_A Data	RANGE_B Data	RANGE_C Data	RANGE_D Data
ENTER: 1: Direct Detection Ps = Ps 2: Homodyne Detection Ps > Ps 3: Heterodyne Detection Ps > Ps 4: Heterodyne Detection Ps = Ps		3	3	3	3
SOURCE PARAMETERS					
ENTER: Device Manufacturer Type Wavelength (nm, um) Cant. Radius Wave (yes/no) Single longitudinal mode (yes/no) Single transverse mode (yes/no) Rated Output Power (W, mW) Threshold Current (I _{th} , mA) Forward Current (I _f , mA) Rise Time (Tr, ns) Relative Intensity Noise (RIN, dB/Hz) Linearity (dB) Spectral Width (nm, um) Vert. X Hor. Angle (deg. X deg.)		INCRAS Laser MEL 50004 1.30 yes no yes 20.00 20.00 1.00 -200.00 20.00 4.00 30 X 30			
Coherence Length (LC, m)		0.07E+00	0.07E+00	0.07E+00	0.07E+00
TYPE OF PHOTODETECTOR		Dual-Balanced	Dual-Balanced	Dual-Balanced	Dual-Balanced
ENTER: 1: Single-Ended 2: Dual-Balanced Excess Noise Suppression (Exs, dB)		2	2	2	2
PHOTODETECTOR PARAMETERS					
ENTER: Photodetector: Manufacturer Type Wavelength (nm, um) Quantum Efficiency (eta) Avalanche Gain (A) Excess Noise Factor (F) Surface Leakage Current (IS, nA) Dark Current (ID, nA) Temperature (T, K) Capacitance (C, pF) Gain-Bandwidth (GB, GHz) Characterization Voltage (V, Volts) Maximum Forward Current (A, mA) AF00		INCRAS PIN Mitsubi MT110 1.30 0.20 1.00 0.00 0.00 300.00 2.00 2.00 10.00 1.00 0.01	INCRAS PIN Mitsubi MT110 1.30 0.20 1.00 0.00 0.00 300.00 2.00 2.00 10.00 1.00 0.01	INCRAS PIN Mitsubi MT110 1.30 0.20 1.00 0.00 0.00 300.00 2.00 2.00 10.00 1.00 0.01	INCRAS PIN Mitsubi MT110 1.30 0.20 1.00 0.00 0.00 300.00 2.00 2.00 10.00 1.00 0.01
FRONT-END PARAMETERS					
ENTER: Noise Figure (F, dB) Load Resistance (RL, Ohms) Stray Capacitance (Cs, pF) Transimpedance Gain (AV, Ohms) System Bandwidth (BW, MHz) Maximum Received Power (Pr, dBm) Background Radiation (Pr, W)		0.0 1000.0 1.00 1.00E+09 10.0 0.00E+00	0.0 1000.0 1.00 1.00E+09 10.0 0.00E+00	0.0 1000.0 1.00 1.00E+09 10.0 0.00E+00	0.0 1000.0 1.00 1.00E+09 10.0 0.00E+00
Responsivity (Ri, mA/W) Dark Current Noise (Idn, nA/Hz) Thermal Current Noise (ITN, nA/Hz) Noise Equivalent Power (NEP, W/Hz) Photon Rate (hp, /s) Bandwidth (Brc, MHz)		7.0E-01 4.4E-02 5.7E-08 6.0E-14 4.4E+05 1.3E+03	7.0E-01 4.4E-02 5.7E-08 6.0E-14 4.4E+05 1.3E+03	7.0E-01 4.4E-02 5.7E-08 6.0E-14 4.4E+05 1.3E+03	7.0E-01 4.4E-02 5.7E-08 6.0E-14 4.4E+05 1.3E+03
COHERENT FRONT-END PARAMETERS					
ENTER: Local Oscillator Power (Po, W) Mixing Efficiency (ME) Autocorrelation Length (LA, m)		0.00E+00 1.00 0.00	0.00E+00 1.00 0.00	0.00E+00 1.00 0.00	0.00E+00 1.00 0.00
Autocorrelation (R(t))		1.0E+00	1.0E+00	1.0E+00	1.0E+00
Received Optical Power Pr, dBm		CNR, dB	CNR, dB	CNR, dB	CNR, dB
	-30	15.8	15.8	15.8	15.8
	-29	17.8	17.8	17.8	17.8
	-28	19.7	19.7	19.7	19.7
	-27	21.7	21.7	21.7	21.7
	-26	23.7	23.7	23.7	23.7
	-25	25.7	25.7	25.7	25.7
	-24	27.7	27.7	27.7	27.7
	-23	29.6	29.6	29.6	29.6
	-22	31.6	31.6	31.6	31.6
	-21	33.6	33.6	33.6	33.6
	-20	35.5	35.5	35.5	35.5
	-19	37.4	37.4	37.4	37.4
	-18	39.3	39.3	39.3	39.3
	-17	41.3	41.3	41.3	41.3
	-16	43.1	43.1	43.1	43.1
	-15	44.9	44.9	44.9	44.9
	-14	46.7	46.7	46.7	46.7
	-13	48.5	48.5	48.5	48.5
	-12	50.2	50.2	50.2	50.2
	-11	51.9	51.9	51.9	51.9
	-10	53.5	53.5	53.5	53.5
	-9	55.1	55.1	55.1	55.1
	-8	56.6	56.6	56.6	56.6
	-7	58.1	58.1	58.1	58.1
	-6	59.5	59.5	59.5	59.5
	-5	60.8	60.8	60.8	60.8
	-4	62.1	62.1	62.1	62.1
	-3	63.3	63.3	63.3	63.3
	-2	64.5	64.5	64.5	64.5
	-1	65.7	65.7	65.7	65.7
	0	66.9	66.9	66.9	66.9
	1	68.0	68.0	68.0	68.0
	2	69.1	69.1	69.1	69.1
	3	70.2	70.2	70.2	70.2
	4	71.2	71.2	71.2	71.2
	5	72.3	72.3	72.3	72.3
	6	73.3	73.3	73.3	73.3
	7	74.3	74.3	74.3	74.3
	8	75.3	75.3	75.3	75.3
	9	76.4	76.4	76.4	76.4
	10	77.4	77.4	77.4	77.4

Ps is the power in each beam reaching the photodetector. Since there are two photodetectors in this dual-balanced system, the total power into the Mach-Zehnder Electric-Field Sensor must also be at least 4Ps. Thus, the performance at 0 dBm corresponds to a minimum input power of 4 mW. However, because half the power is not wasted in the substrate, the CNR is improved by 3 dB, and is largely immune to degradation from excess intensity noise.

Table VI -- CNR for dual-balanced detection

Fiberdyne Optoelectronics. The highlighted items are the more important parameters that affect the CNR. Table V gives the analysis for a single-ended detection system. For a negligible excess noise of -200 dBc/Hz, as shown in Range_A, the CNR is 63.9 dB for a received optical power of 1 mW.

The CNR drops to 50.8 dB for an excess noise of -140 dBc/Hz. The corresponding graph, Figure 22, shows this reduction in CNR and the dynamic range in a more dramatic way. This reduced CNR may present a major barrier in obtaining the desired dynamic range. The effect of intensity noise could be decreased by using complementary photodetection. To do this, the Mach-Zehnder interferometer would require two output ports instead of one. This is accomplished by the addition of a directional coupler at the output of the Mach-Zehnder as shown in Figure 23.

The signals applied to dual photodetectors are complementary. As the phase in one branch of the interferometer varies, the intensity on one photodetector increases while on the other photodetector it decreases. Both detectors have the same received intensity noise if the interferometer is in phase quadrature. Thus, while the difference signals between the photodiodes due to the phase-induced intensity changes add, since they are equal and opposite, the common mode intensity noise cancels. Typically, with careful design, up to 30 or more dBs of intensity noise suppression can be obtained. This dual-detection receiver also has the advantage that the half of the optical power that was previously wasted in the substrate is now available at the additional photodetector. Thus, while the electrical signal power detected by the front-end is four times larger, the shot noise is twice as large, leading to a net improvement in CNR of 3 dB.

Table VI gives this analysis for a complementary detection system providing 30 dB of intensity noise suppression. For negligible excess noise, the CNR now increases by 3 dB to 66.9 dB. Even when the RIN is significant, the CNR is only slightly reduced by 0.1 dB. This is practically identical to the results obtained from the shot noise limited expression shown below.

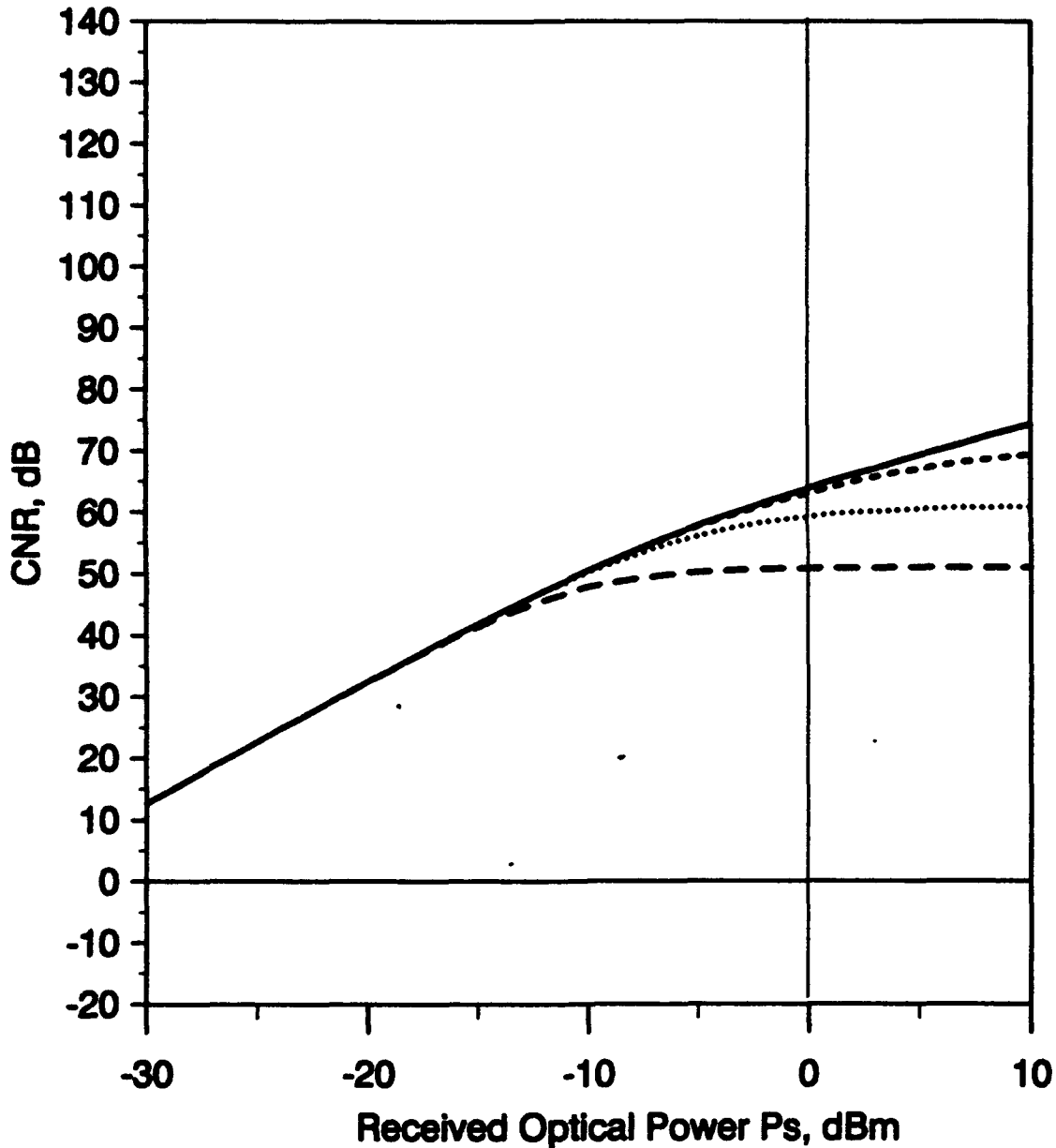
$$CNR = \frac{2\eta e P_s}{hf_c B_n} \quad (44)$$

This indicates that the optical front-end is shot noise limited for $P_s = 1$ mW. The accompanying graph, Figure 24, demonstrates this more clearly. Single mode laser diodes are likely to have less intensity noise because of the lack of mode competition effects.

Figure 22

CNR IN HOMODYNE OPTICAL SYSTEMS

Single-Ended Detection



 RIN = -200 dBc/Hz RIN = -160 dBc/Hz RIN = -150 dBc/Hz RIN = -140 dBc/Hz

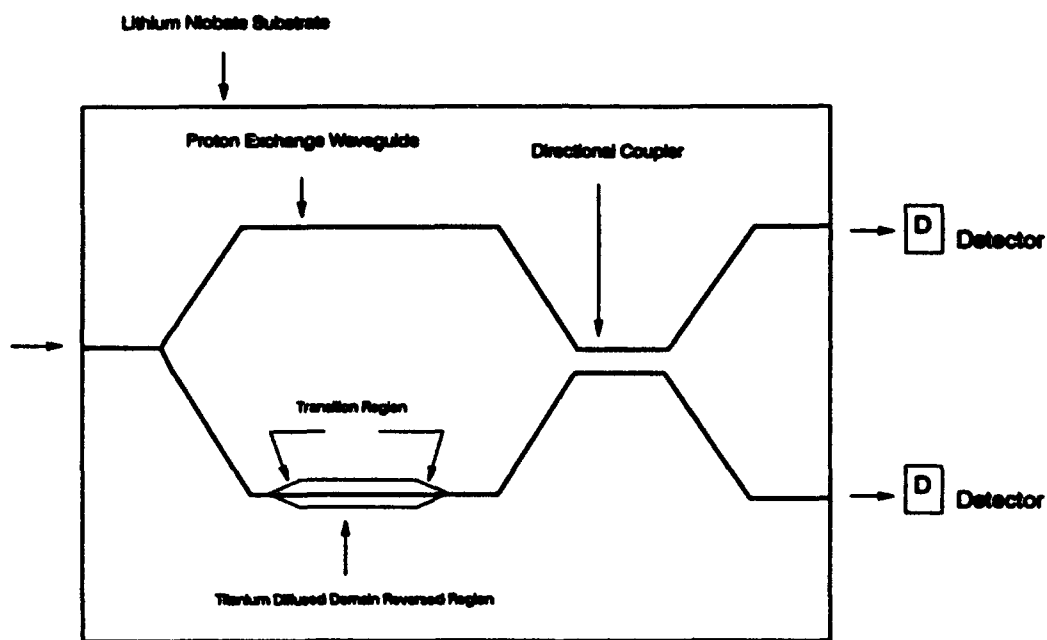
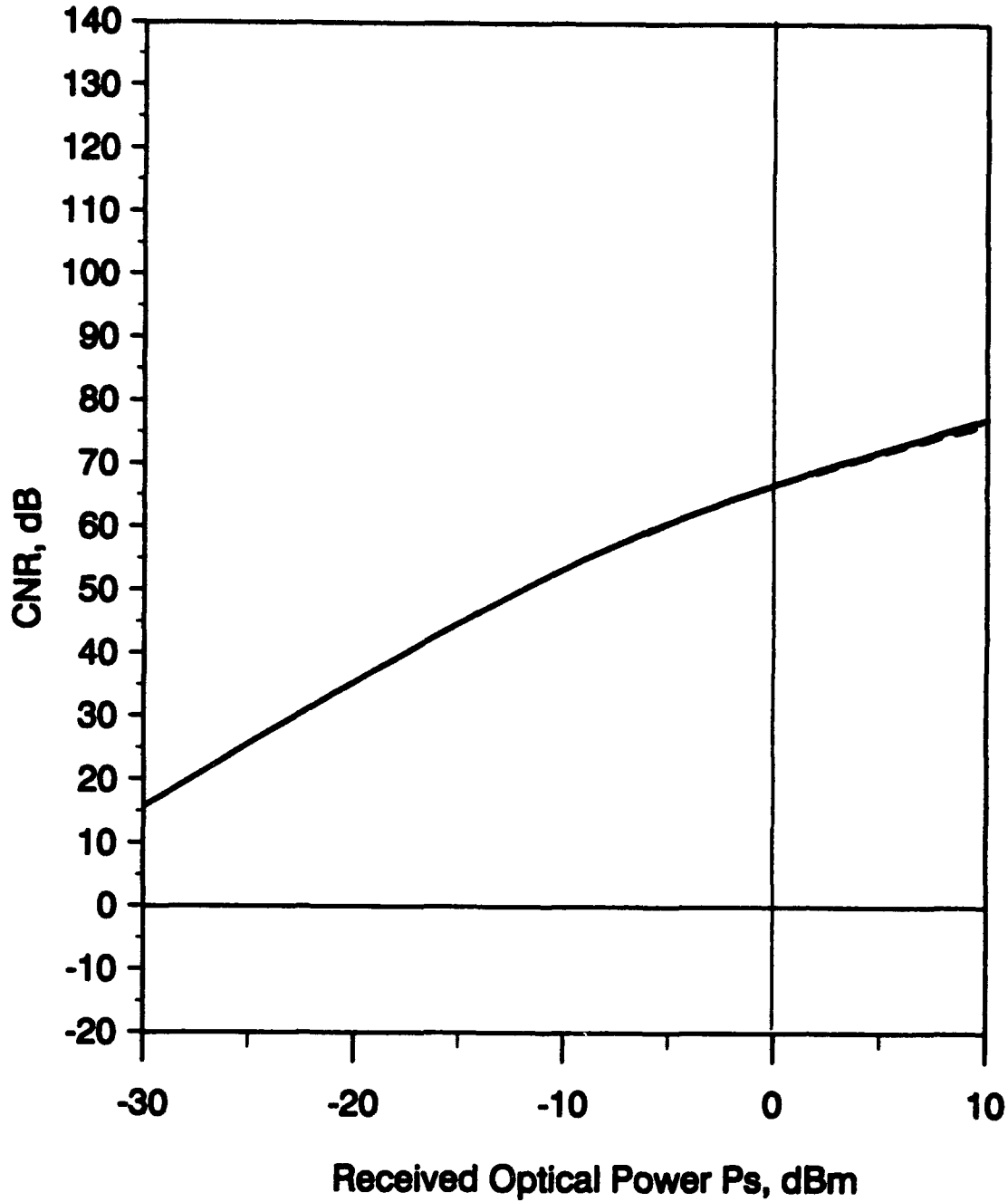


Figure 23. Mach-Zehnder interferometer with dual-balanced detector

Figure 24

CNR IN HOMODYNE OPTICAL SYSTEMS

Dual-Balanced Detection



 RIN = -200 dBc/Hz RIN = -180 dBc/Hz RIN = -150 dBc/Hz RIN = -140 dBc/Hz

LINEARITY ANALYSIS

This section deals with the harmonic distortion caused by exciting the electric field sensor by two frequencies ω_1 and ω_2 of equal amplitudes. The second and third harmonics and the intermodulation frequency will be analyzed. The dynamic range is limited by the intermodulation term because it produces a higher level of distortion than the third harmonic.

The input/output relationship for the electric field sensor is given by

$$\frac{P_o}{P_i} = \frac{1}{2} [1 + \cos(\phi_o + \phi_m(\sin \omega_1 t + \sin \omega_2 t))] \quad (45)$$

where ϕ_o = bias point of the modulator,
 ϕ_m = peak phase deviation produced due to the field.

This expression can be expanded with a power series into individual harmonic and intermodulation terms. The resulting modulation ratios are¹⁴:

Modulation ratio at the fundamental frequency, ω :

$$\frac{\phi_m \sin \phi \left[(-1) + \frac{3(\phi_m)^2}{8} - \frac{5(\phi_m)^4}{96} \right] \sin \omega t}{1 + \cos \phi \left[1 - \frac{\phi_m^2}{2} + \frac{3(\phi_m)^4}{32} \right]} \quad (46)$$

Modulation ratio at the second harmonic frequency, 2ω :

$$\frac{\frac{(\phi_m)^2}{4} \cos \phi \left[1 - \frac{(\phi_m)^2}{3} \right] \cos 2\omega t}{1 + \cos \phi \left[1 - \frac{\phi_m^2}{2} + \frac{3(\phi_m)^4}{32} \right]} \quad (47)$$

Modulation ratio at the third harmonic frequency, 3ω :

¹⁴S.A. Wilcox and M.D. Drake, "Practical system design considerations for wideband fiber optic links using external modulators", SPIE 933, pp. 234-239 (1988).

$$\frac{\frac{(\phi_m)^3}{24} \sin \phi \left[(-1) + \frac{5(\phi_m)^2}{16} \right] \sin 3\omega t}{1 + \cos \phi \left[1 - \frac{\phi_m^2}{2} + \frac{3(\phi_m)^4}{32} \right]} \quad (48)$$

Intermodulation ($2\omega_2 - \omega_1$):

$$\frac{\frac{(\phi_m)^3}{8} \sin \phi \left[1 - \frac{5(\phi_m)^2}{24} \right] \sin (2\omega_2 - \omega_1)t}{1 + \cos \phi \left[1 - \frac{\phi_m^2}{2} + \frac{3(\phi_m)^4}{32} \right]} \quad (49)$$

These modulation ratios are plotted in Figures 25 and 26 as a function of modulator bias point for a peak phase deviation of 0.10 and 0.25 radian. At quadrature bias, the second harmonic disappears and the dynamic range is limited only by the intermodulation distortion. As the bias point deviates from quadrature, the second harmonic term rises rapidly. Referring to the graph for 0.25 radian, the second harmonic rises to the level of intermodulation for a bias drift of 7 degrees. Beyond this, the second harmonic term severely degrades the dynamic range. For a peak deviation of 0.1 radian, the second harmonic rises to the level of the intermodulation term for a bias drift of 3 degrees. As the peak deviation increases, there is less demand on the stability requirements for quadrature bias.

The peak phase deviation allowed will depend on the criterion for distortion. The criterion selected to limit the peak phase deviation is when the intermodulation distortion term equals the noise floor level. Based on Eqs. (46) - (49), the modulation ratios of the fundamental and the intermodulation terms are plotted at quadrature bias as a function of peak phase deviation. Figure 27 shows that the noise floors for optical powers of 1 and 10 mW are horizontal lines. The graph indicates that the maximum phase deviations allowed are 0.172 and 0.115 radian for optical powers of 1 and 10 mW, respectively.

If small bandwidth such as 10 kHz is used to analyze the spectrum of the electromagnetic energy received, there is no dynamic range problem. However, to "capture" the signature of a complex random electromagnetic waveform containing frequency components approaching 1 GHz, a detection bandwidth of 1 GHz would be required.

Figure 25

Theoretical Modulation Ratio

Peak Deviation = 0.1 rad

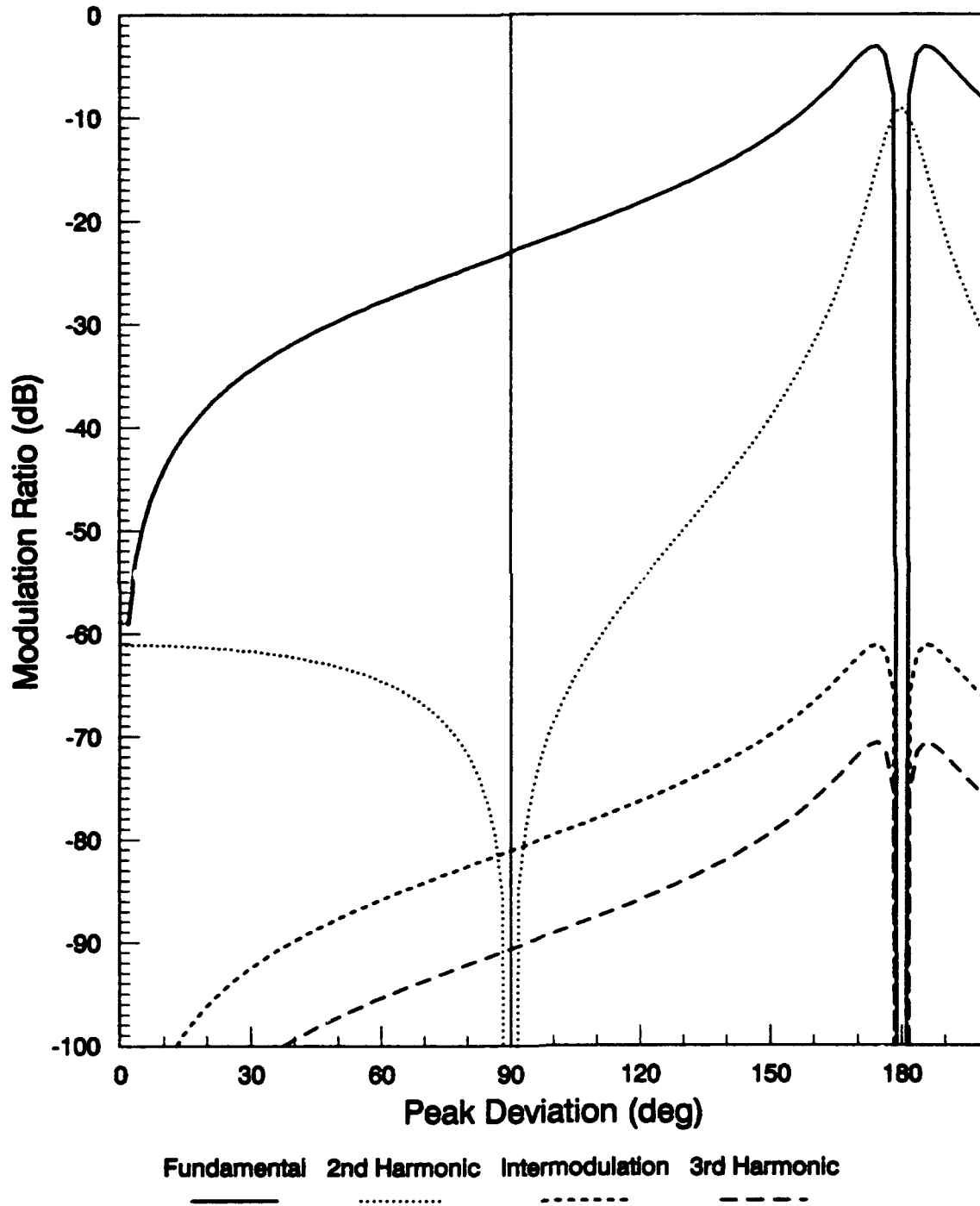
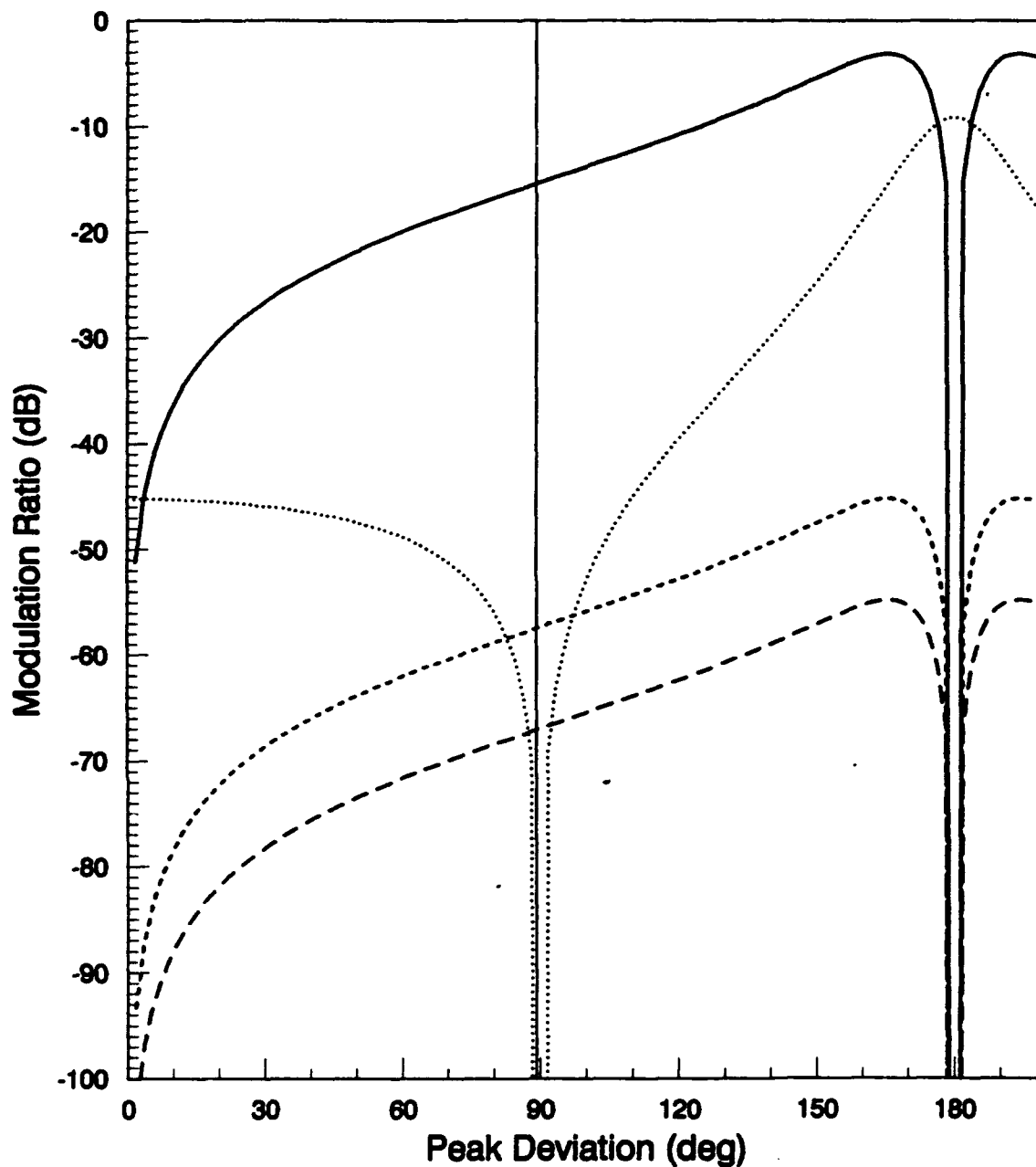


Figure 26

Theoretical Modulation Ratio

Peak Deviation = 0.25 rad



Fundamental 2nd Harmonic Intermodulation 3rd Harmonic

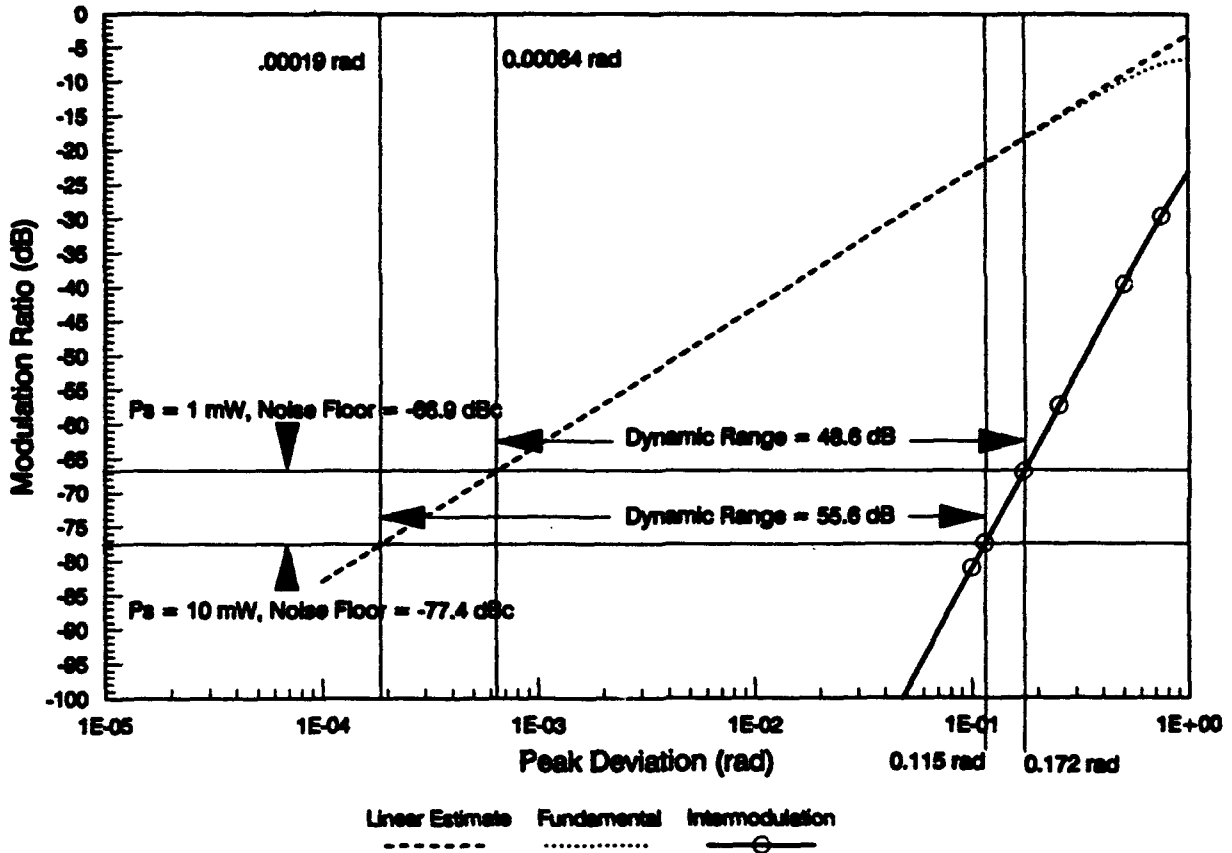
— ····· - - - - - · - · -

Figure 27

Interferometer Response - Quadrature Bias

Signal Bandwidth = 1 GHz

Wavelength = 1.3 Microns



SNR ANALYSIS

The relationship among signal-to-noise ratio (SNR), phase modulation index (ϕ_0) and the carrier-to-noise ratio (CNR) is:

$$SNR = \frac{\Delta\phi^2}{2} CNR \quad (50)$$

All phase deviations are peak values.

For $P_s = 1$ mW, i.e., $P_{in} \geq 2$ mW, and a maximum phase deviation of 0.172 radian, expressed in dB format:

$$\begin{aligned} SNR &= CNR - 18.3 \text{ dB} \\ &= 48.6 \text{ dB} \end{aligned}$$

For $P_s = 10$ mW, i.e., $P_{in} \geq 20$ mW, and a maximum phase deviation of 0.172 radian:

$$\begin{aligned} SNR &= CNR - 21.8 \text{ dB} \\ &= 55.6 \text{ dB} \end{aligned}$$

For $P_s = 10$ mW, the CNR is 77.4 dB for a 1.57 GHz noise equivalent bandwidth. The minimum detectable phase deviation is obtained when the SNR = 0 dB. For a 1.57 GHz noise equivalent bandwidth, the minimum detectable peak phase deviation is:

$$\phi_{0, min} = 1.9 \times 10^{-4} \text{ radian}$$

For $P_s = 1$ mW, and a 1.57 GHz noise equivalent bandwidth,

$$\phi_{0, min} = 6.4 \times 10^{-4} \text{ radian}$$

An electric field 40 dB above these values required to produce a signal at this noise floor level would produce a peak phase deviation several dBs below the maximum phase deviation calculated above.

DYNAMIC RANGE ANALYSIS

Analyses of dynamic range are shown in Figures 28 and 29 for a dual-detection system. The SNR penalty produced by phase deviations of 0.172 and 0.115 radian for 1 and 10 mW received per channel and the noise floors for the different RIN levels are shown as horizontal lines.

Figure 28
Relative Signal Levels
For 1 mW Dual-Balanced Detection

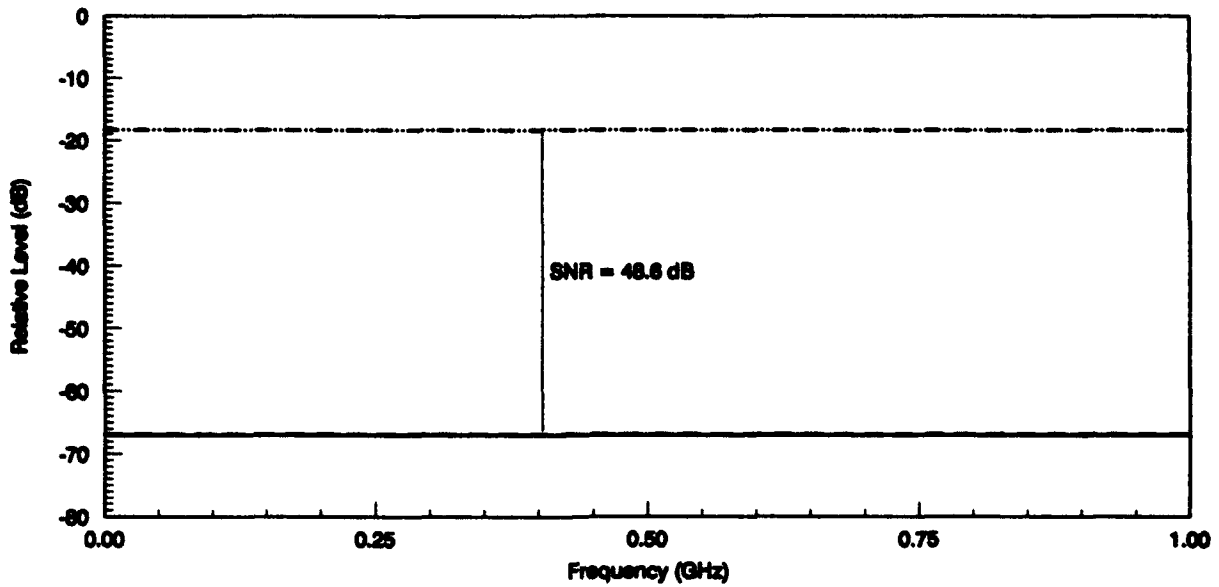
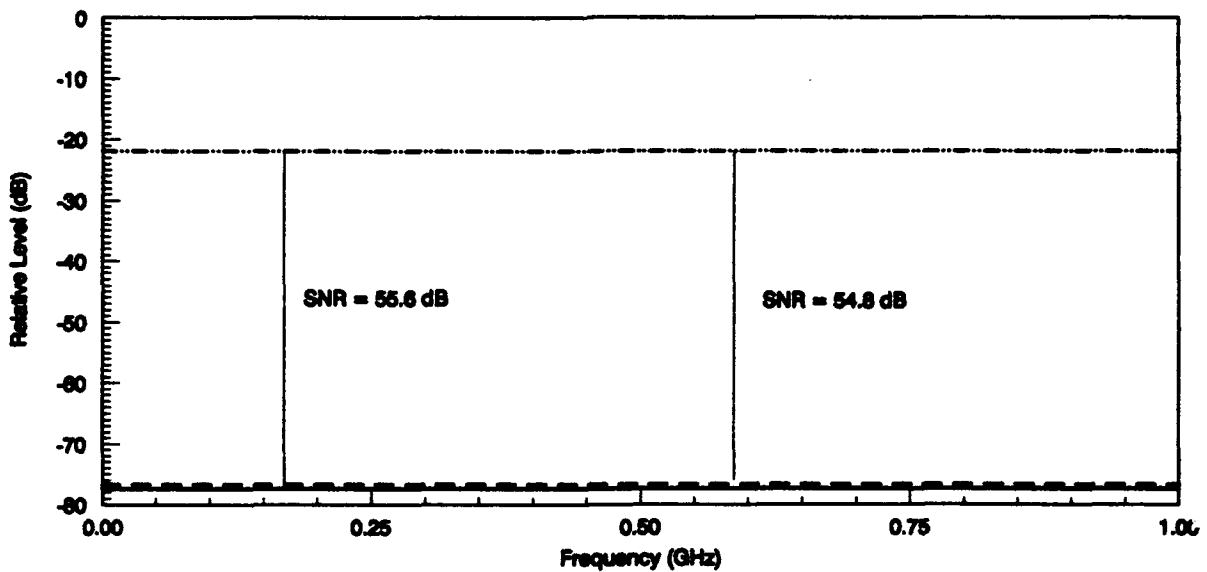


Figure 29
Relative Signal Levels
For 10 mW Dual-Balanced Detection



RIN = -200 dBc
 CNR = -77.4 dBc

RIN = -160 dBc
 CNR = -77.4 dBc

RIN = -150 dBc
 CNR = -77.3 dBc

RIN = -140 dBc
 CNR = -76.6 dBc

Peak Dev = 0.115 rad
 Signal = -21.8 dB

At a power level below 1 mW, it may be difficult to maintain shot noise limited detection consistent with the required 1 GHz system bandwidth and with the use of PIN photodetectors. The graphs produced from Tables V and VI show that below $P_s = 0$ dBm (1 mW), the optical receiver starts to become kT noise limited. A good rule of thumb for a high quality PIN photodetector is that for a photodetector load of 1k ohm, about 1 mW of total power ($2P_s$) is required to achieve the threshold of quantum noise limited detection. It is not possible to increase the load much above this value without compromising the bandwidth. It would be better to avoid using APDs, particularly for the dual-detection system. At these reduced power levels it probably becomes less of a necessity to consider complementary photodetection, unless the excess noise is very large.

The choice of single or dual-detection depends on the RIN values for commercial 1300 nm lasers. If a complementary photodetection system is not used, a laser with a cut off frequency considerably in excess of 1 GHz will be required. This must be done to ensure that the low frequency wing of the relaxation peak, which can be accompanied by more than 80 dB/Hz of excess noise, does not raise the noise floor near the 1 GHz system -3 dB frequency.

SENSITIVITY ANALYSIS

There are two main differences between the electroded and the electrode-less device. First, the dielectric constant of lithium niobate, is greater than that of free space and, thus, tends to "short out" the electric field. Second, the conventional dipole antenna has a voltage induced on it which is then applied to closely spaced electrodes on a substrate. A very large localized field is thus produced in an electroded device. Hence, the electric field "seen" by the electrode-less Mach-Zehnder interferometer will be substantially less than for the device with electrodes.

This poses no problem for detecting Electro Magnetic Pulse (EMP), which mainly covers the spectral range 10 kHz to 100 MHz and has peak field strengths of 50 kV/m. Indeed, the presence of discrete metallic electrodes could cause electrical breakdown of the device. Without electrodes, the electric field may be allowed to greatly exceed the dynamic range limitations of the device without causing failure or damage to the rest of the electrical system. Moreover, the device is less likely to disturb the field being measured.

The electric field generated by lightning strikes is generally much lower than that produced by EMP, but the duration is much longer. Electro Magnetic Pulses typically have rise times on the order of 10 ns, whereas lightning strikes have rise times of about 6 μ s and a field strength of up to 1000 V/m at a range of 1 km.

In a Mach-Zehnder interferometer without electrodes, the electric field "seen" by the device will be different from the free space electric field because of the permittivity of the electro-optic material. The device effectively acts as a capacitor in series with two free space capacitors. The dielectric constant of lithium niobate is approximately 35. Thus, the field experienced by the substrate is reduced by a factor of about 35.

The sensitivity of the device and its dimensions can be determined for a maximum electric field which produces a peak deviation based on linearity conditions. The device constant K is given by

$$K = \frac{\pi}{V_x}. \quad (51)$$

V_x for a push-pull interferometer is given by

$$V_x = \frac{\lambda}{2 n_o^3 r_{33}} \frac{d}{L} \quad (52)$$

for $\lambda = 1.3\mu\text{m}$, $n_o = 2.15$, $r_{33} = 30.8 \times 10^{-12}$,
 $L = 1 \text{ mm}$ and $d = 1 \text{ mm}$, $V_x = 2000 \text{ Volts}$.

For a phase deviation ϕ , the voltage across the electro-optic material is

$$V_{\text{LiNbO}_3} = \frac{\phi}{K}. \quad (53)$$

The electric field inside the crystal is

$$E_{\text{LiNbO}_3} = \frac{V_{\text{LiNbO}_3}}{d} \quad (54)$$

The free space electric field is a factor of 35 greater than that in the crystal. Table VII illustrates the sensitivity calculations based on Eqs. (51) - (54). The calculations are shown for a crystal thickness of 0.5 mm and two different interaction lengths of 10 and 25 mm. The peak deviations for two different optical power levels of 1 and 10 mW are 0.172 and 0.115 radian, respectively. The electric field values are that of free space.

The 25 mm long device is capable of providing a sensor with a noise floor of 570 V/m for an optical power of 1 mW. This device length is reasonable for fabrication and will easily satisfy the frequency response requirements of 1 GHz. The optical source power required would be 2 mW for a lossless device. In practice, losses due to

fiber coupling and scattering are about 3 dB. Hence, a source power of 4 to 5 mW would be required. Such laser sources are currently available in the market.

Table VII

SENSITIVITY CALCULATIONS

Wavelength = 1.3 μ m
 Bandwidth = 1GHz

Complementary detection using dual photodetectors at the output.

d mm	L mm	V _r Volts	P _s mW	ϕ_{min} rad	E _{min} V/m	ϕ_{max} rad	E _{max} V/m
0.5	10	100	1	.00064	1.4x10 ³	.172	3.8x10 ⁵
0.5	25	40	1	.00064	567	.172	1.5x10 ⁵
0.5	10	100	10	.00019	424	.115	2.6x10 ⁵
0.5	25	40	10	.00019	168	.115	1.0x10 ⁵

FREQUENCY RESPONSE

The frequency response is limited primarily by the transit time of the optical beam through the device interaction length. The crystal's response to a microwave field is instantaneous on the time scale of a microwave period. The microwave period must be much longer than this transit time through the interaction region for the device to see a static electric field. As the microwave frequency increases, the optical beam sees a field that is the average of the instantaneous field over the transit time. Were the microwave period to equal the transit time, the optical beam would see no net field, hence, no net phase change. Mathematically, the condition for the upper frequency limit on the microwave signal may be expressed as^{15,16}:

$$2f_m \tau < 1 \quad (55)$$

where, f_m = highest microwave frequency
 τ = transit time of the optical beam through the interaction region.

τ is given by

$$\tau = \frac{L}{(c/n)} \quad (56)$$

where, L = length of the interaction region
 c = velocity of light (3×10^8 m/sec)
 n = refractive index of LiNbO_3 = 2.15 at $1.3 \mu\text{m}$ wavelength).

Based on the above equations, the highest frequency of operation is calculated as follows:

$L \leq 70 \text{ mm}, f_m = 1 \text{ GHz}$
 $L \leq 23 \text{ mm}, f_m = 3 \text{ GHz}$
and $L \leq 2.3 \text{ mm}, f_m = 30 \text{ GHz}$

The device interaction length plays a major role in determining the frequency response and detection capability. A sensor device having an interaction length of 25 mm could operate from DC to 1 GHz with adequate sensitivity for a signal bandwidth of 1 GHz.

¹⁵W.F. Filter et. al., "Photonic measurements of microwave pulses", SPIE 566, pp. 227-232 (1985).

¹⁶J. Jarzynski and R.P. De Paula, "Fiber optic electric field sensor technology", SPIE 718, pp. 48-55 (1986).

The extremely short interaction length of 2.3 mm required to achieve a sensor bandwidth of 30 GHz would require an optical power of 100 mW to obtain sensitivity comparable to the 3 GHz device. An alternate approach would be to use the technique of phase reversed segments^{17,18} in which the device bandwidth could be increased without sacrificing sensitivity.

We will first describe the periodic phase reversal technique in which the center frequency is shifted to 30 GHz. The device bandwidth is typically limited to less than 10%, in this example, 3 GHz. Figure 30 illustrates a Mach-Zehnder interferometer in which segments of domain inverted regions are located in the two legs of the interferometer. The length of each segment is calculated based on the center frequency. For a center frequency of 30 GHz, the length L is chosen to be 2.3 mm as per the calculations of Eqns. (55) and (56). The phase reversed segments are separated by a distance traveled by the optical signal in the waveguide during one half cycle of the microwave signal. The period of a 30 GHz signal is 33.33 psec, during which time the optical signal travels 4.6 mm in a LiNbO₃ waveguide.

The device shown in Figure 30 operates as follows. Suppose the microwave signal is in its positive cycle and a phase of ϕ_0 when the optical signal enters the segment A. As the optical beam travels through the segments A_1 and A_2 , it experiences equal and opposite phase shifts $\pm\phi$, respectively. The segment spacing is such that as the optical signal enters segments B_1 and B_2 , the microwave signal is in its negative cycle at a phase of $\pi + \phi_0$. Since the electric field is now reversed, the segments B_1 and B_2 also experience $\pm\phi$, phase shifts respectively. This is because a positive electric field generates a positive phase shift in A_1 and a negative phase shift in B_1 and vice versa. Hence, every segment in the lower and upper leg of the interferometer contributes a phase shift of $+\phi$, and $-\phi$, respectively. If there are "n" segments in each leg of the interferometer, the total phase at the output is $2n\phi$.

The device shown in Figure 30 has ten segments in each leg of the interferometer for a total length of 23 mm. The segment length of 2.3 mm yields a center frequency of 30 GHz. The device bandwidth is that of an interferometer in which the interaction length is 23 mm, i.e., 3 GHz.

¹⁷Rod C. Alferness et. al., "Velocity-matching techniques for integrated optic traveling-wave switch/modulators", IEEE Journal of Quantum Electronics QE-20, pp. 301-309 (1984).

¹⁸M. Nazarathy et. al., "Velocity-mismatch compensation in traveling-wave modulators using pseudorandom switched-electrode patterns", J. Opt. Soc. of Amer. 4, pp. 1071-1079 (1987).

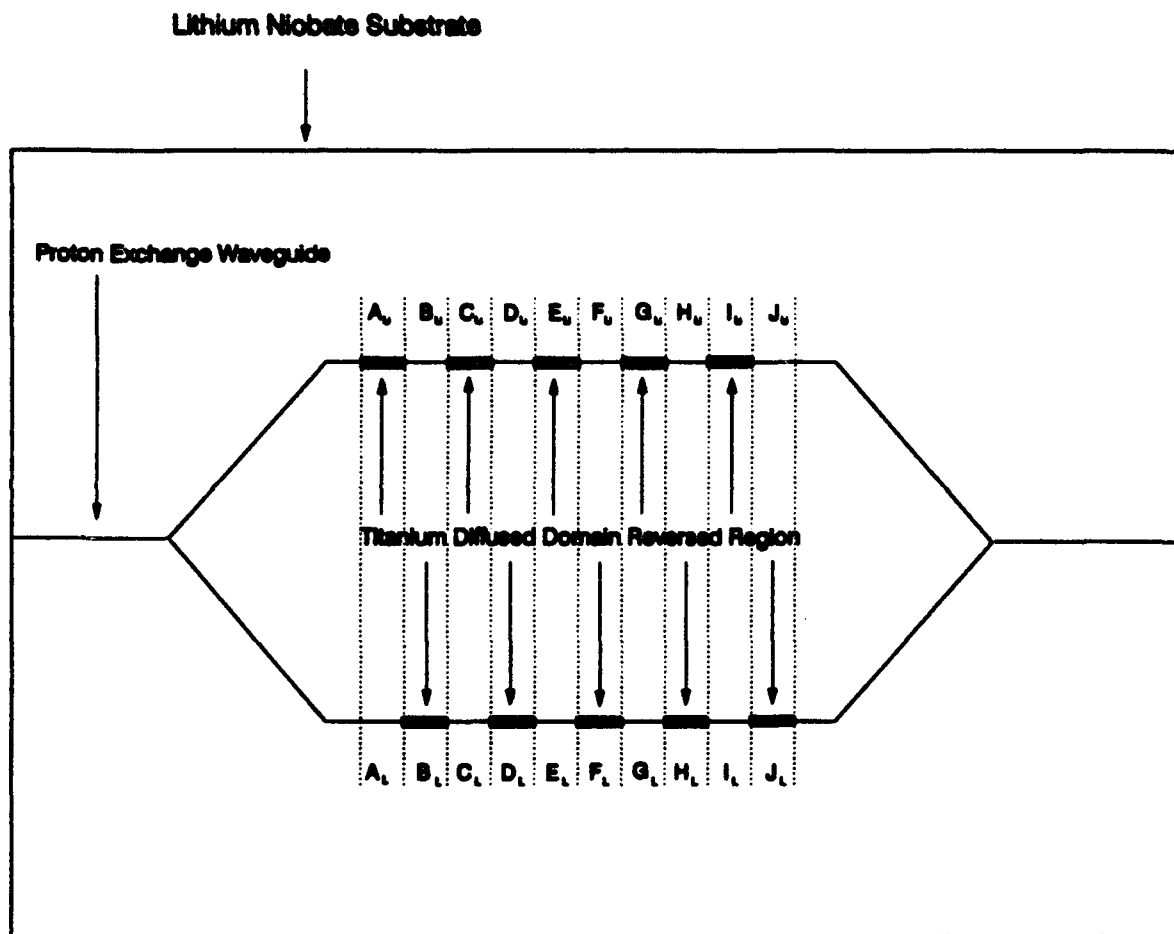


Figure 30. Periodic phase reversal technique to increase the device operating frequency to 30 GHz

The electric field seen by the optical beam is the average of the instantaneous field over the transit time. If the transit time is equal to half the microwave period, as is the case in this example, the electric field seen by the optical beam is only 65% compared to a static electric field. This implies that the phase shift experienced by the ten segment interferometer above is equivalent to that of a device having a 15 mm long interaction region.

The periodic phase reversed design described above is a narrow band device that exhibits a bandwidth of 10%, i.e., 3 GHz for a 30 GHz center frequency. A broadband device could be designed in which the segment lengths are chosen based on a pseudorandom Barker code¹⁸. This could yield highly sensitive broadband devices operating from DC to 40 GHz. This design exhibits a non-linear phase response and is, therefore, applicable only in pulse applications.

ELECTRIC FIELD SENSOR CALIBRATION

When calibrating and testing electric field sensors devised for operation at a few GHz, it will be quite convenient to use small Crawford TEM cells. However, at 30 GHz, the wavelength in air is only 1 cm, and this presents a problem in producing a very compact TEM cell with the desired uniform field characteristics. The cell would have to be so small that the packaged device would not be able to fit into it. The problem is with the transverse dimension of the cell and not with its length. These cell dimensions will have to be smaller than the wavelength in order that there is only one mode within the cell and that the field is uniform.

There are two choices:

1. We can construct a miniature TEM cell cavity and test the sensor in its unpackaged form, i.e., just the device and its attached fiber optic leads.
2. Test the packaged device but in free space. This would require the use of an anechoic chamber.

The first option has the disadvantage that the package itself is likely to modify the response of the sensor. Hence, to test the device without its packaging may give unreliable results. The second option has the disadvantage of having to set up a transmitting antenna that can produce an accurate electric field over a wide frequency range. It is not inconceivable that the frequency calibration might be a two-step process. Over lower frequencies, a conventional TEM cell could be used, while at high frequencies an anechoic chamber would be employed. This divide and conquer approach would have the advantage that the anechoic chamber would only be used at the highest frequencies, and thus could be relatively small.

Instruments For Industry, IFI, manufactures a Crawford Cell TEM Test Chamber, Model No. CC110, which may be used between DC and 1 GHz. The first resonance, where the wavelength is equal to the distance between the top plate and the septum, is above 1 GHz. The test chamber has inside dimensions of 4.7" X 7.1", more than adequate for the packaged sensor. The manufacturer gives a maximum recommended test object size of 2.36" X 2.36" X 0.75" (60 mm X 60 mm X 18 mm). The length of the unpackaged 1 GHz sensor is the same as the maximum test object length. This company could custom build a more compact TEM cell to take the resonance frequency to about 2 GHz.

Figure 31 shows the three basic ways of calibrating the TEM cell. Method (a) uses an amplified wideband noise source, whose intensity is measured with a spectrum analyzer via the output of the electric field sensing system. Method (b) uses a tracking generator to give a swept amplitude response of the sensor.

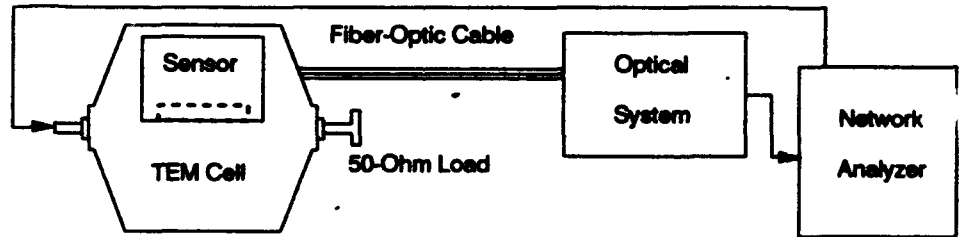
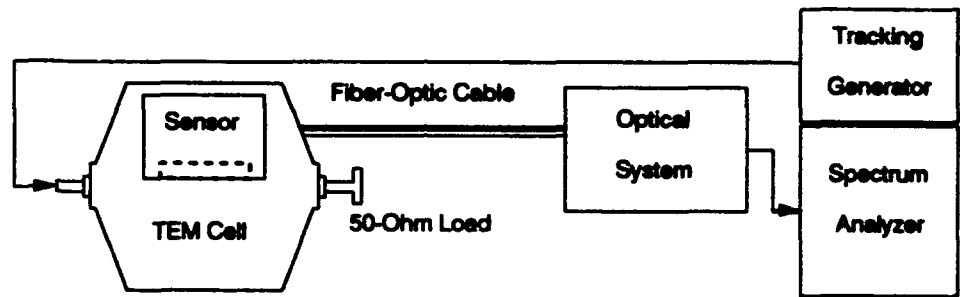
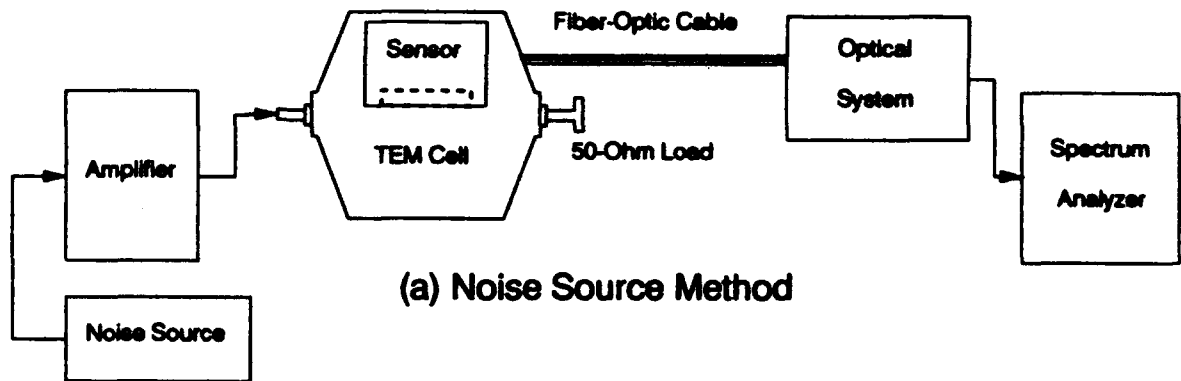


Figure 31. Schematic for calibrating the electric field sensor

Method (c) uses a network analyzer to obtain the amplitude and phase response of the sensor.

Scheme (a) shows how a wideband radio frequency noise source can be used to calibrate the sensor. The output of the device is amplified up to a level that can properly modulate the electric field sensor via the TEM cell. The bandwidth of the device is indicated by the noise density profile (envelope) as displayed on the spectrum analyzer. Of course, this scalar technique provides no information about the sensor's phase response.

Scheme (b) shows the preferred technique which uses a tracking generator driven by the spectrum analyzer. This also is a scalar measurement and doesn't yield any information about the device's phase response. The tracking generator is a swept signal generator whose frequency is provided by a local oscillator that is common to both it and the spectrum analyzer. In this way, at any instant of time, the frequency to which the spectrum analyzer is tuned, is the same frequency being put out by the tracking generator. Thus, the intensity of the received signal directly correlates with the amplitude response of the device under test.

One of the most important pieces of test instrumentation in this program is the spectrum analyzer. This will be used for designing and testing major optical components in the system, e.g., the laser source and photodetector, and calibrating the sensor in a TEM cell. All aspects of the laser source and photodetector noise performance can be checked in the frequency domain. The tracking generator facility allows swept amplitude measurements and, in conjunction with another signal generator, gives us the capability to perform some limited two-tone intermodulation tests.

Scheme (c) shows the more sophisticated system that can yield the phase response. The Network Analyzer measures both the amplitude and phase response. The typical resolution of a microwave Network Analyzer is 100 kHz. This corresponds to the I.F. bandwidths employed in these systems, and is also about the resolution bandwidths that will be employed in the spectrum analyzer systems. Such bandwidths also allow fairly rapid sweep (refresh) rates for spectrum analyzer displays lacking storage capabilities.

TEM CELL PERFORMANCE

The electric field generated by this chamber is given by:

$$E = \frac{V}{D} \quad (57)$$

where D is the septum to top plate separation in meters. In the case of the CC110 TEM cell, this has a dimension of 4.7"/2, i.e.,

2.35" (60 mm). To obtain a field of 1 volt/meter requires a peak voltage of 60 mV, or 42.4 mV r.m.s.. This would be produced by a power of 36 μ W or -14.4 dBm.

The graph shown in Figure 32 is a plot of the electric field produced in the Crawford CC110 TEM Cell as a function of the drive power to the cell, and the phase modulation depth produced within the cell for a given drive power. The electric field, which is indicated by the full line, is read off the left hand ordinate scale. The induced phase deviation, which is indicated by the broken line, is read off the right hand ordinate. From Table VII, Sensitivity Calculations, we see that for a sensor with 1 mW received power at each of the two photodetectors and a Mach-Zehnder interaction length of 25 mm, the minimum detectable electric field in a 1 GHz signal bandwidth would be 570 V/m. To produce this field in the TEM cell would require a drive power of 40.6 dBm, i.e., 11.4 watts. This is positioned slightly off the right hand edge. A drive power of +30 dBm (1 W) produces a field of 168 V/m and a phase deviation of about 1.9×10^{-4} radians. This is about 10.6 dB below the 1 GHz bandwidth noise floor of the system, and is thus not detectable in that bandwidth.

This is not a problem for the calibration procedure since, as we have explained before, for swept frequency calibration purposes we can employ spectrum analyzer or network analyzer bandwidths much less than 1 GHz. If the detection bandwidth was 100 kHz, then the signal-to-noise ratio and sensitivity would increase by a factor of 50 dB. This means that the drive power requirements for a minimum detectable signal could be reduced by 50 dBm. The TEM cell would only require a drive power of -9.4 dBm. In practice, we would likely drive the TEM cell at about +20 dBm (100 mW) to ensure a clean, low-noise signal. If need be, we could use resolution bandwidths as small as 1 kHz.

DYNAMIC RANGE TESTS

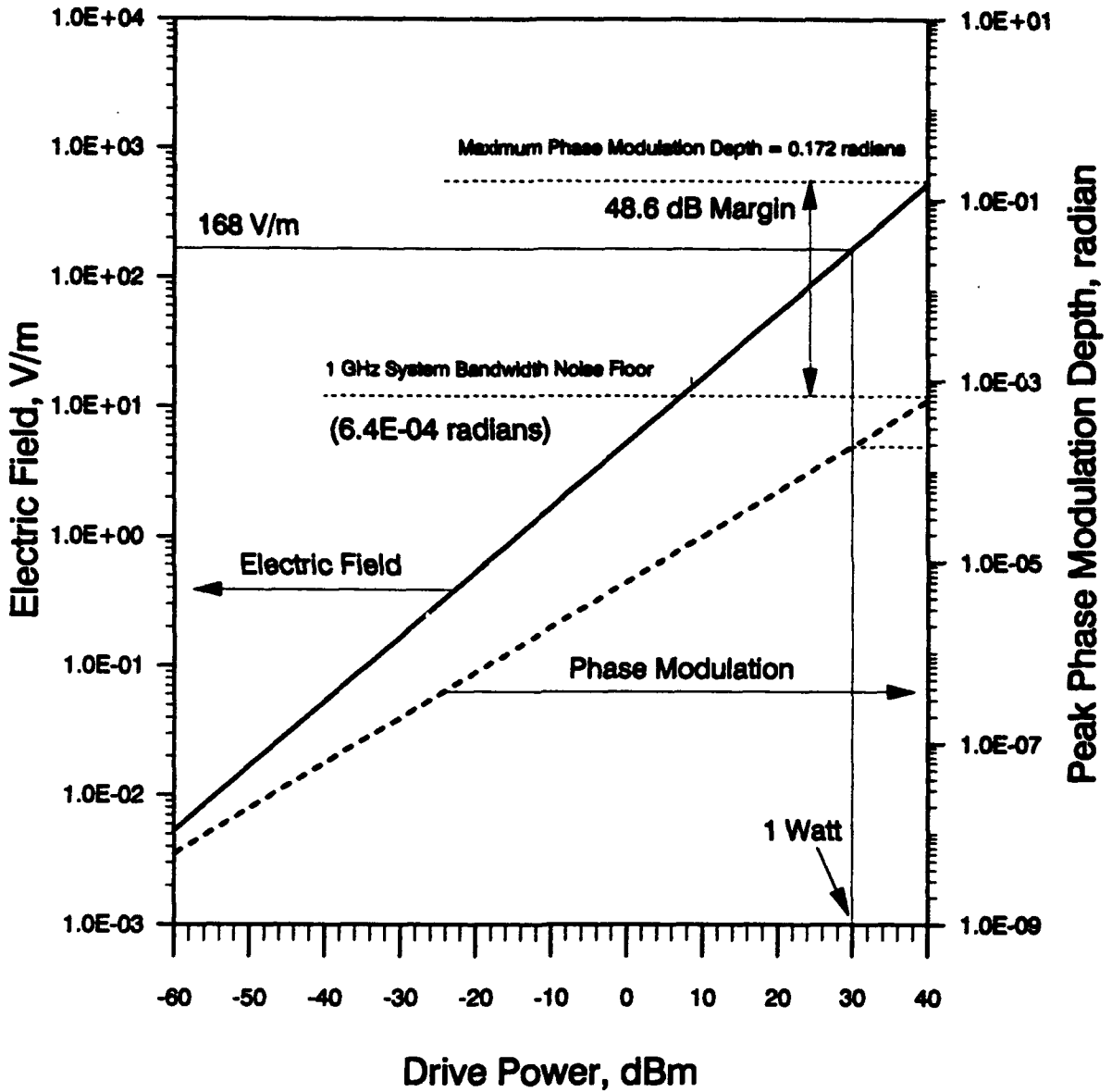
In order to exercise the device over some dynamic range, it would appear that we shall need to use a small RF power amplifier so that powers of up to about 20 W (+43 dBm) may be applied. Based on linearity considerations, the dynamic range is limited to a maximum electric field of 150,000 V/m. Clearly, we are not going to be able to produce or sustain such a CW field of this magnitude, or even a pulsed field. The weakest links in the system would probably be the connectors. At high frequencies, powers of about 100 W (+50 dBm) probably represent the limit. This corresponds to electric fields in this TEM cell of about 1.7 kV/m -- still very small compared to the 150 kV/m limit of the device (0.172 radians). A lightning or EMP simulating test facility would be required to fully test the device.

Figure 32

ELECTRIC FIELD & PEAK PHASE MODULATION DEPTH
AS A FUNCTION OF TEM CELL DRIVE POWER

IFI Crawford Cell Test Chamber Type CC110

1 mW Dual-Balanced Detection



Assumes 50-ohm cell termination

Electric Field

Phase Deviation

—————

- - - - -

Of course, at low frequencies very high fields could be produced with close parallel plates. A voltage of 150 volts across a 1 mm gap will produce an electric field of 150 kV/m. This should be a good way of testing the dynamic range properties of the device at lower frequencies, without concerns about the frequency response, since the intermodulation behavior should be independent of frequency. A two-tone test, from two MHz-type R.F. generators (frequencies f_1 and f_2) can be used for this test. R.F. coils, or transformers, can be used to better impedance-match the plate intermodulation test system to the 50-ohm signal generators. Typically, $f_1 = 10$ MHz, and $f_2 = 11$ MHz, so we would be looking for intermodulation product frequencies of $2f_1 \pm f_2$ and $2f_2 \pm f_1$, i.e., 9 MHz, 12 MHz, 31 MHz, and 32 MHz. A 100 kHz I.F. resolution would easily discriminate (separate) the 9 MHz and 12 MHz products from the 10 MHz and 11 MHz tones.

It should be noted that in order to "see" the third order intermodulation in a 1 GHz bandwidth, we need to apply an electric field voltage considerably in excess of 150 kV/m. However, since we will be using narrow band detection, i.e., 100 kHz, we can see intermodulation products 50 dB lower down than would be the case for a 1 GHz bandwidth, where the dynamic range, as set by the third-order intermodulation is 48.6 dB. This is equivalent to saying that the CNR is improved by 50 dB. For small distortion, these products are proportional to $(\phi_n)^3$, so that a 50 dB noise floor reduction may be compensated by a reduction in ϕ_n by a factor of 46.4. Thus, the visibility of third order intermodulation distortion for $\phi_n = 0.172$ radians in a 1 GHz bandwidth is the same as for $\phi_n = 3.7 \times 10^{-3}$ radians in a 100 kHz bandwidth. At the same time, with its reduced deviation, the signal level has fallen by 16.7 dB. The signal to distortion level in this situation is now about $48.6 - 16.7 + 50 = 82$ dB. This figure happens to be close to the limits on the ability of most spectrum analyzers to show both the signal and intermodulation products simultaneously on the same logarithmic display. Of course, whether or not both the signal and intermodulation products can still be displayed simultaneously, does not affect our ability to measure each signal and signal product.

We have already seen that a +30 dBm (1 Watt) drive power to the TEM cell produces a field of 168 V/m, and a phase modulation $\phi_n = 1.9 \times 10^{-6}$ radians. Thus, even the Crawford cell can manage some limited intermodulation tests. Only a test that exercises the device over π radian of phase excursion can really test the sensor's linearity. Its large scale non-linearity may not be identical to its small scale non-linearity if the cosine-squared phase discriminator (interference) characteristic is itself non-uniform. Also, since we would like to see the effect on intermodulation of bias drift, this can only be done effectively for large phase deviations.

APPLICATIONS

A schematic of the sensor instrument for the remote measurement of electric field or voltage is shown in Figure 33. Several applications for the electric field sensor are listed below.

- **Measurement of high power microwave (HPM) sources** - The sensor could be used to detect leakage from industrial-grade radio frequency (RF) heating and sealing systems. RF heating systems are used in manufacturing, food processing and semiconductor industries. Recently, there has been an increasing public awareness of the potential health hazard of electromagnetic radiation. This issue is presently undergoing review by the EPA. Other applications exist in measuring the fields produced by commercial RF transmitters and antennas to monitor their output and potential health hazard.
- **Measurement of high power, pulsed, non-repetitive microwave sources** - Possible applications are detection of high power radar and electronic counter measure (ECM) signals.
- **Measurement of fields produced by high altitude electromagnetic pulse (HEMP) simulators** - Based on these calculations, the insulation strength of high voltage transmission lines could be designed to protect them from HEMP-induced flashover. The sensor could also be used in real time to monitor passage of electrical storms in the vicinity of power lines.
- **Lightning protection for aircrafts by incorporating the sensor in their skins** - Aircrafts traditionally have used metal skins which act as a Faraday cage to protect the electronics inside them. Composite materials are increasingly being used in modern aircrafts which make them highly susceptible to damage from lightning strikes. The aircraft can obtain advance warning of atmospheric conditions to avoid electrical storms.
- **Remote measurement of electric field and voltage in hazardous and hostile environments** - The sensor is intrinsically safe since it carries no current or voltage. Hence, it will not generate any sparks in hazardous or explosive environments. Since the sensor is electrically isolated, it cannot induce any electrical breakdown.

- **Near-field strength measurement for antennas and radars on naval ships** - The sensor could be used to optimize the transmission efficiency and to ensure that naval personnel are not subjected to hazardous levels of electromagnetic fields.
- **Remote antenna from the shelter** - The sensor could be placed in a forward position to the receiving antenna to detect enemy counter measures. The information could then be transmitted by fiber optic links to a remote shelter for automatic protection of sensitive receivers.
- **Medical and biological research in the measurement of electrical fields** - The sensor could be employed in the test chamber to monitor and map the fields. Since this is a non-metallic sensor it will not disturb the fields.
- **Measurement of electric field and voltage in power systems** - The sensor could be used in high voltage environments which are subject to a large amount of electrical interference.

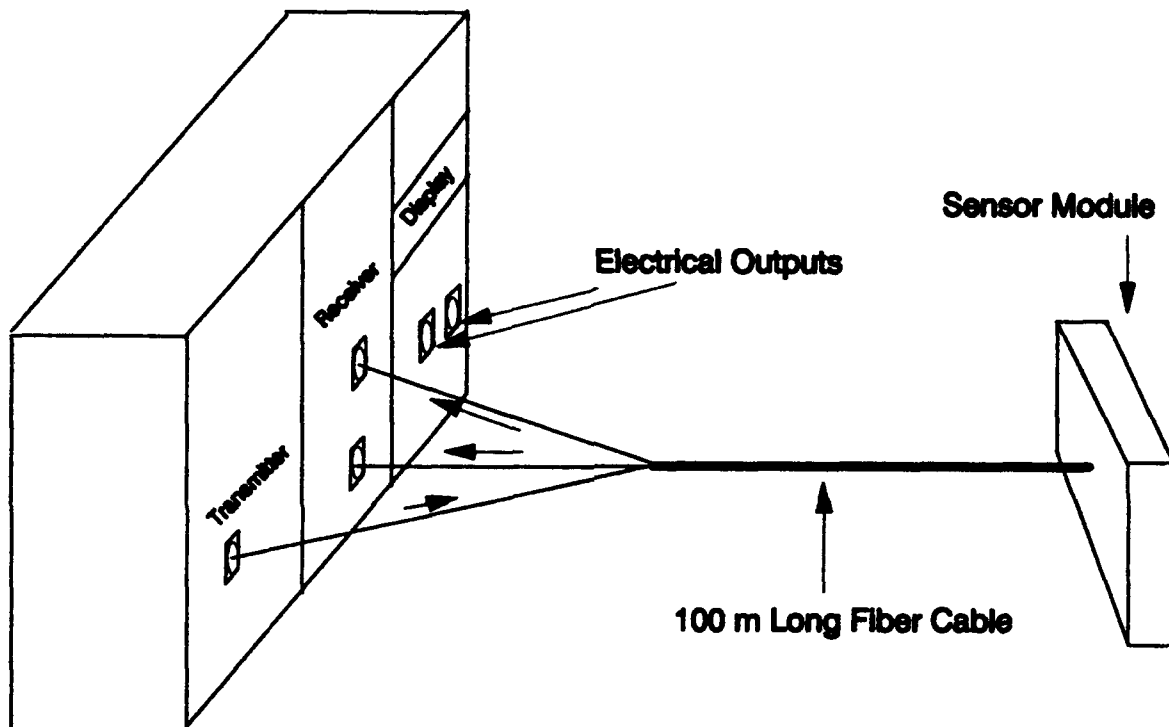


Figure 33. Schematic of a configuration for the remote measurement of electric field or voltage

CONCLUSIONS AND RECOMMENDATIONS

This program has successfully demonstrated the feasibility of developing a nonmetallic electromagnetic field sensor based on optical interferometers in a lithium niobate electro-optic crystal. This is an all-dielectric sensor instrument that consists of optical fibers for input and output to the electro-optic crystal. Thus, the sensor is free from interference from electromagnetic fields.

The technique of selective reverse poling using titanium diffusion in lithium niobate was proposed and demonstrated. This is a novel method to manufacture the sensor and SRICO intends to make an application for a United States Patent.

Our analysis indicates that the electric field sensor is feasible, and we recommend a Phase II SBIR program to develop a prototype sensor instrument. A complete instrumentation package including a laser, a photodetector and signal processing electronics will be developed during the Phase II program. The sensor instrument will be tested and delivered to the U.S. Army Harry Diamond Laboratories. We recommend the following program to develop the prototype sensor instrument.

The objectives of this proposed Phase II effort are:

- to design and develop an electrode-less Mach-Zehnder interferometer for electric field sensing;
- to fabricate a prototype fiber pigtailed sensor device;
- to design and develop a system for testing and calibrating the sensor;
- to develop an instrumentation system incorporating the electric field sensor.

The overall program is divided into two parts -- component development and system development. Tasks 1 - 7, associated with component development, are designed to produce a prototype fiber pigtailed electric field sensor. Tasks 8 - 10, associated with system development, are designed to produce the instrumentation system for the electric field sensor. This Phase II SBIR program is scheduled over a two-year period.

Task 1: Finalize Electric Field Sensor Specifications

A project kick-off meeting will be held with the project manager to finalize the performance requirements of the sensor.

Task 2: Finalize Electric Field Sensor Design

The electric field sensor as per the specifications in task 1 will be fabricated in a lithium niobate substrate to operate at a laser wavelength of 1.3 μm . In this task, the waveguide design will be finalized for the creation of the drawings to produce the photomasks. The waveguide will consist of several test patterns and the Mach-Zehnder interferometer.

Task 3: Fabricate Electric Field Sensor for Laboratory Testing

The sensor will be fabricated using the photomasks developed in task 2. Sub-tasks include:

Substrate Preparation - The substrate purchased from the vendor will be cleaned prior to domain inversion and waveguide fabrication steps.

Domain Inversion - Titanium metal strips will be delineated for diffusion to produce selective domain inverted regions in the crystal.

Waveguide Fabrication - An aluminum metal mask will be developed on top of a lithium niobate crystal to act as a barrier in the proton exchange waveguide process.

End-Face Polishing - The end-faces will be polished for coupling light in and out of the waveguide.

The output of this task will be several waveguide samples to be used for testing.

Task 4: Evaluate Electric Field Sensor

Light from a 1.3 μm laser will be coupled to a single mode polarization maintaining optical fiber. The fiber output will thus be coupled to the optical waveguide fabricated in the crystal. At the output, a microscope objective will be used to focus the light onto a photodiode. The output of this task will be the establishment of the parameters for the final device design.

Task 5: Finalize Prototype Electric Field Sensor Design

Based on the results of task 4, the prototype design will be completed. In this task, the waveguide design will be completed for the creation of the drawings to produce the photomasks. The photomask will consist of the design of single and two-ended Mach-Zehnder interferometer sensor devices.

Task 6: Fabricate Prototype Electric Field Sensor

The sensor will be fabricated using the photomasks developed in task 5. The process parameters used to fabricate the sensor will be modified based on the results of the laboratory device. Sub-tasks include the same as those of task 3. Additional sub-tasks are:

Dice Crystal - The crystal sample will consist of 20 or more sensor devices. The crystal will be cut into individual devices or dies to facilitate fiber attachment and packaging.

Attach Optical Fibers - Single mode optical fibers will be attached to the input and output ports of the sensor device. The input port will be attached to a polarization maintaining single mode optical fiber. The output port will be attached to standard communication-type single mode fibers.

The output of this task will be two fiber-pigtailed sensor devices that will be available for testing and evaluation.

Task 7: Package Prototype Electric Field Sensor

The fiber pigtailed sensor devices will be packaged in a non-metallic enclosure. The package will be designed to protect the fiber and waveguide interface from accidental damage. The packaging material will be selected to withstand the various environmental operating conditions.

Task 8: Design and Fabricate Optoelectronic Package

This task will address the laser requirements, the electronics for driving the laser and the signal processing electronics for converting the modulated optical signal to an RF signal. Sub-tasks include:

Laser Selection - The laser will be selected based on the optical power required to achieve the desired dynamic range. Various laser manufacturers will be evaluated to obtain a low noise laser. Considerations will be given to ease of attaching a polarization maintaining fiber to the laser source.

Laser Power Supply Selection - Laser power supplies are available from several manufacturers. The power supply will be chosen based on stability and its ability to supply the required drive current.

Optical Detector Selection - The detector will be required to have a bandwidth greater than 1 GHz. In addition, the two-ended Mach-Zehnder interferometer will require a package that has two detectors in it.

Packaging and Systems Integration - The optoelectronic package will be assembled to contain the laser, the detector and the associated electronics within it.

Fiber Optic Cable Fabrication - The fiber optic cable linking the electric field sensor to the instrumentation package will contain a single mode polarization maintaining fiber and two communication grade single mode fibers. If a suitable cable system is not available commercially, we will arrange to have a special cable made.

The output of this task is an instrumentation package that will provide optical input to the sensor and receive and process the signal from the electric field sensor.

Task 9: Develop Calibration Techniques for the Electric Field Sensor

A TEM cell will be designed or a commercial unit modified and interfaced with instrumentation for evaluating the sensor device.

Task 10: Evaluate Prototype Electric Field Sensor

In this task we will evaluate the packaged sensor device. The TEM cell developed in task 9 will be used to evaluate system parameters. Sub-tasks include:

System Calibration - The device sensitivity will be measured to obtain sensor calibration curves.

Noise Floor Measurement - The minimum detectable electric field will be measured with a signal generator applied to the TEM cell and a spectrum analyzer.

Intermodulation Distortion (Dynamic Range) - By applying two frequencies, the sensor's dynamic range will be measured.

Frequency Response Measurement - The TEM cell will be driven by a Network Analyzer or a Tracking Generator. Swept frequency techniques will be employed to characterize the sensor over a 1 GHz bandwidth. At frequencies below 2 GHz, a conventional TEM cell could be used, while at high frequencies an anechoic chamber would be required.

Task 11: Delivery / Reporting

A complete prototype sensor unit will be delivered to Harry Diamond Laboratories, at the end of the program, for testing and evaluation. Brief monthly reports, a final report and a final briefing detailing the work carried out during this Phase II effort will be provided.



OFFICE OF THE UNDER SECRETARY OF DEFENSE (ACQUISITION)
DEFENSE TECHNICAL INFORMATION CENTER
CAMERON STATION
ALEXANDRIA, VIRGINIA 22304-6145

EPLY
EFER TO

DTIC-OCF (703) 274-6847 (DSN) 284-6847
A O W93-1751

25 Oct 93

SUBJECT: Request for Scientific and Technical Report

TO: Director
U.S. Army Research Laboratory
Attn: AMSRL-OP-CI-AD
2800 Powder Mill Road
Adelphi, MD 20783-1145

1. We have been unable to locate the report referenced below in the Defense Technical Information Center Collection. In accordance with DoDD 3200.12 "DoD Scientific and Technical Information Program" the Defense Technical Information Center is to receive two copies of the Technical Report cited below.

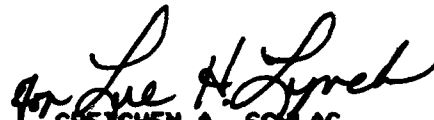
Please return letter
with report.

2. All copies of the report must be suitable for reproduction including a clearly marked distribution statement as described in DoDD 5230.24. (See reverse side for categories of distribution statement.) A clearly marked loan copy suitable for reproduction is acceptable.

3. If for any reason you cannot furnish the report, please return the copy of this letter annotating your reason on the reverse side.

4. A mailing label for shipping the reports and a DTIC Form 50 to obtain the AD number after processing are enclosed.

FOR THE ADMINISTRATOR:


GREYCHEN A. SCHLAG

Chief, Collection Division

2 Encl

1. Mailing Label
2. DTIC Form 50

W93-1751

Subject: Optical Interferometers for Sensing Electromagnetic Fields.

DAAL02-90-C-0078 NOTE: DTIC would appreciate receiving all technical reports generated on cited contract, including interim, progress, final, etc. If the contracts results were only published in a medium such as proceedings, thesis, or journal article, please forward.

Enclosure (1) provides information on this particular work unit.

hm/93-298

30041

PLEASE CHECK THE APPROPRIATE BLOCK BELOW:

- 2 copies are being forwarded. Indicate whether Statement A, B, C, D, E, F, or X applies.
- DISTRIBUTION STATEMENT A:
APPROVED FOR PUBLIC RELEASE: DISTRIBUTION IS UNLIMITED
- DISTRIBUTION STATEMENT B:
DISTRIBUTION AUTHORIZED TO U.S. GOVERNMENT AGENCIES ONLY; (Indicate Reason and Date). OTHER REQUESTS FOR THIS DOCUMENT SHALL BE REFERRED TO (Indicate Controlling DoD Office).
- DISTRIBUTION STATEMENT C:
DISTRIBUTION AUTHORIZED TO U.S. GOVERNMENT AGENCIES AND THEIR CONTRACTORS; (Indicate Reason and Date). OTHER REQUESTS FOR THIS DOCUMENT SHALL BE REFERRED TO (Indicate Controlling DoD Office).
- DISTRIBUTION STATEMENT D:
DISTRIBUTION AUTHORIZED TO DOD AND U.S. DOD CONTRACTORS ONLY; (Indicate Reason and Date). OTHER REQUESTS SHALL BE REFERRED TO (Indicate Controlling DoD Office).
- DISTRIBUTION STATEMENT E:
DISTRIBUTION AUTHORIZED TO DOD COMPONENTS ONLY; (Indicate Reason and Date). OTHER REQUESTS SHALL BE REFERRED TO (Indicate Controlling DoD Office).
- DISTRIBUTION STATEMENT F:
FURTHER DISSEMINATION ONLY AS DIRECTED BY (Indicate Controlling DoD Office and Date) or HIGHER DOD AUTHORITY.
- DISTRIBUTION STATEMENT X:
DISTRIBUTION AUTHORIZED TO U.S. GOVERNMENT AGENCIES AND PRIVATE INDIVIDUALS OR ENTERPRISES ELIGIBLE TO OBTAIN EXPORT-CONTROLLED TECHNICAL DATA IN ACCORDANCE WITH DOD DIRECTIVE 5230.25, WITHHOLDING OF UNCLASSIFIED TECHNICAL DATA FROM PUBLIC DISCLOSURE, 6 Nov 1984 (Indicate date of determination). CONTROLLING DOD OFFICE IS (Indicate Controlling DoD Office).
- This document was previously forwarded to DTIC on _____ (date) and the AD number is _____.
- In accordance with the provisions of DoD Instructions, the document requested is not supplied because: _____
- It is TOP SECRET.
- It is excepted in accordance with DoD instructions pertaining to communications and electronic intelligence.
- It is a registered publication.
- It is a contract or grant proposal, or an order.
- It will be published at a later date. (Enter approximate date, if known.)
- Other. (Give Reason.) _____

John Latus
Authorized Signature Date

JOHN LATUS
Print or Typed Name
3008
(703) 490-8371
Telephone Number

ACCESSION NUMBER: DA319867 ACCESSION DIGRAPH: DA ACCESSION SEQ NBR: 319867 TRANS. TYPE: M STATUS OF EFFORT: T PERF. METHOD: C
PERF. TYPES: R SUMMARY DATE: 20 APR 1993 PRECEDING DATE: 27 FEB 1992 START DATE: JUN 1990 END DATE: MAR 1994
EFFORT CLASS CODE: (U) EFFORT ADD. NOTICE: RECORD CLASS. CODE: (U) RECORD ADD. NOTICE: (U)

CLASSIFICATION AUTHORITY: REGRADING DATE: REGRADING EVENT: REGRADING CODE: DISTR. CODE: C

TITLE: OPTICAL INTERFEROMETERS FOR SENSING ELECTROMAGNETIC FIELDS LOCAL CONTROL NO: 000
SUB RECORD INDICATOR: LINKING ACCESSION NO: MISSION AREA CODES:
SEARCH DATA: B0M40B;B0B40D;B0M40F DOD SUBJ CATEGORIES: 0905, 1706

FUNCTION CODES: TECH CODES: SOURCE CODE: 424569
RESP. ORG ACTIVITY NAME: ARMY RESEARCH LAB ADELPHI MD

RESP. ORG COMPONENT NAME: OFFICE SYMBOL: ANSRL-WT-ND TELEPHONE NO: 703-490-2313 DSN NO:
RESP. ORG LOCATION: ADELPHI MD 20783 GEOPOL: 2405 SOURCE CODE: 422325

RESP. INDIVIDUAL: LATESS, J OFFICE SYMBOL: ANSRL-WT-ND TELEPHONE NO: 703-490-2313 DSN NO:
PERF. ORG ACTIVITY NAME: SRICO OPTICAL ENGINEERING POWELL OH

PERF. ORG COMPONENT NAME: SRICO OPTICAL ENGINEERING PETWORTH COURTH
PERF. ORG LOCATION: POWELL OH 43065 GEOPOL: 3912
PERF. ORG PRINCIPAL INVEST: SRIRAM, S OFFICE SYMBOL: TEL NO: 614-848-3239 DSN:

ASSOC. INVESTIGATORS:
0609502A, 1L985502NM40, 0000

FY	AMOUNT	WRK	YRS	FY	AMOUNT	WRK	YRS
--	-(K\$)-	-----	----	--	-(K\$)-	-----	----
90	00001	00.0					
91	00001	00.0					

ROLLUP INDICATORS:
CONTRACT/GRANT NO: DAAL0290C0078 CONTRACT EFFECTIVE DATE: 01 JUN 1990 CONTRACT EXPIRATION DATE: 31 JAN 1991

CONTRACT FACE VALUE (IN K\$): 49 CONTRACT CUMULATIVE TO DATE (IN K\$): 49 PRODUCT INDICATOR: N
DOMESTIC TECH TRANS: HI S & A CATEGORIES:

SPECIAL STUDIES SUBJ:
ACTIVITY CODE: ANDH PRIM PROJ SERIAL NO: M40 INTERNAT SOURCES: ISNA PROCESS DATE: 29 APR 1993 RECEIPT DATE: 27 APR 1993

THRUST INDICATORS:

KEYWORDS: SBIR, OPTICAL INTERFEROMETER, ELECTRIC FIELD SENSOR, PERIODICALLY POLED, INTEGRATED OPTICS
DESCRIPTORS: (U) CRYSTALS, DETECTORS, DUAL CHANNEL, ELECTRIC FIELDS, ELECTRODES, ELECTROMAGNETIC FIELDS, FIELD EQUIPMENT, INTEGRATED SYSTEMS, INTERFEROMETERS, LASERS, METALS, MODULATION, NUMBERS, OPTICAL DETECTORS, OPTICAL EQUIPMENT, OPTICAL INTERFEROMETERS, OPTICAL WAVEGUIDES, OPTICS, SEARCHING, SUBSTRATES, TIME, WAVEGUIDES

OBJECTIVE: (U) SEARCH NUMBERS: BOM408; BOM40D; BOM40F; BOM41C. DESIGN AND BUILD A TOTALLY DIELECTRIC, MINIATURE, WIDEBAND, OPTICAL ELECTRIC FIELD SENSOR.

APPROACH: (U) UTILIZE AN INTEGRATED OPTICAL WAVEGUIDE DEVICE CONFIGURED AS A MACH-ZEHNDER INTERFEROMETER TO MODULATE A LASER PROPORTIONAL TO A TIME VARYING ELECTRIC FIELD.

PROGRESS: (U) A TECHNIQUE HAS BEEN ESTABLISHED WHEREBY A MACH-ZEHNDER INTERFEROMETER CAN BE PRODUCED WITH THE CRYSTAL SUBSTRATE OF THE TWO INTERFEROMETER WAVEGUIDE CHANNELS OPPOSITELY POLED. THIS WILL PERMIT MODULATION OF THE LASER WITHOUT THE METALLIC ELECTRODES NORMALLY REQUIRED IN THESE MODULATION DEVICES.

END